

1 **Spatial heterogeneity effects on land surface modeling of**
2 **water and energy partitioning**

3 Lingcheng Li, Gautam Bisht, L. Ruby Leung

4 Atmospheric Sciences and Global Change Division, Pacific Northwest National Laboratory,
5 Richland, WA, USA

6
7 Correspondence to: Lingcheng Li (lingcheng.li@pnnl.gov)

Deleted: 1

Deleted: 1

Deleted: 1

Deleted: 1

12 **Abstract**

13 Understanding the influence of land surface heterogeneity on surface water and energy fluxes is
14 crucial for modeling earth system variability and change. This study investigates the effects of four
15 dominant heterogeneity sources on land surface modeling, including atmospheric forcing (ATM),
16 soil properties (SOIL), land use and land cover (LULC), and topography (TOPO). Our analysis
17 focused on their impacts on the partitioning of precipitation (P) into evapotranspiration (ET) and
18 runoff (R), partitioning of net radiation into sensible heat and latent heat, and corresponding water
19 and energy fluxes. An initial set of 16 experiments were performed over the continental U.S.
20 (CONUS) using the E3SM land model (ELMv1) with different combinations of heterogeneous
21 and homogeneous datasets. The Sobol' total and first-order sensitivity indices were utilized to
22 quantify the relative importance of the four heterogeneity sources. Sobol' total sensitivity index
23 measures the total heterogeneity effects induced by a given heterogeneity source, consisting of the
24 contribution from its own heterogeneity (i.e., the first-order index) and its interactions with other
25 heterogeneity sources. ATM and LULC are the most dominant heterogeneity sources in
26 determining spatial variability of water and energy partitioning, mainly contributed by their own
27 heterogeneity and slightly contributed by their interactions with other heterogeneity sources. Their
28 heterogeneity effects are complementary both spatially and temporally. The overall impacts of
29 SOIL and TOPO are negligible, except TOPO dominates the spatial variability of R/P across the
30 transitional climate zone between the arid western and humid eastern CONUS. Accounting for
31 more heterogeneity sources improves the simulated spatial variability of water and energy fluxes
32 when compared with ERA5-Land reanalysis dataset. An additional set of 13 experiments identified
33 the most critical components within each heterogeneity source, which are precipitation,

Deleted: The Sobol' total sensitivity analysis is utilized to quantify the relative importance of the four heterogeneity sources.

Deleted: Results show that

Deleted: , and t

Deleted: Comparison with ERA5-Land reanalysis reveals that a...

Deleted: the

Deleted: sources

Deleted: :

44 temperature and longwave radiation for ATM, soil texture and soil color for SOIL, and maximum

45 fractional saturated area parameter for TOPO.

Deleted: ¶

47 **1. Introduction**

48 **Land surface heterogeneity plays a critical role in the terrestrial water, energy, and**
49 **biogeochemical cycles from local to continental and global scales** (Giorgi and Avissar, 1997;
50 Chaney et al., 2018; Zhou et al., 2019; Liu et al., 2017). As the land component of global Earth
51 System Models (ESMs) and Regional Climate Models (RCMs), land surface models (LSMs) are
52 used to simulate the exchange of momentum, energy, water, and carbon between land and
53 atmosphere. LSMs have been widely utilized in studies focused on climate projection, weather
54 forecast, flood and drought forecast, and water resources management (Clark et al., 2015;
55 Lawrence et al., 2019). At the resolutions typically applied in ESMs and RCMs, LSMs have
56 limited ability to resolve land surface heterogeneity to skillfully represent its impacts on the surface
57 fluxes and subsequent effects on earth system and climate simulations through land-atmosphere
58 interactions. Singh et al. (2015) demonstrated that increasingly capturing topography and soil
59 texture heterogeneity at finer resolutions improves the land surface modeling of soil moisture,
60 terrestrial water storage anomaly, sensible heat, and snow water equivalent. Therefore, better
61 representing spatial heterogeneity in LSMs may be crucial to reliably simulate water and energy
62 exchange between land and atmosphere (Essery et al., 2003; Jr. et al., 2017; Fan et al., 2019; Fisher
63 and Koven, 2020).

64

65 **Several approaches have been developed to resolve land surface heterogeneity in LSMs.** The
66 most common class of method is the tile approach that subdivides each grid into several tiles to
67 account for heterogeneous surface properties (Avissar and Pielke, 1989). The Community Land
68 Model version 5 (CLM5) and the Energy Exascale Earth System Model (E3SM) land model (ELM)
69 utilize a nested subgrid hierarchy in which each grid cell is composed of multiple land units, soil

Deleted: ¶

Deleted: heat

Deleted: representing

Deleted: land surface modeling

74 columns, and plant functional types. Tesfa et al. (2017; 2020) developed a topography-based
75 subgrid structure based on topographic properties such as surface elevation, slope, and aspect to
76 better represent topographic heterogeneity in ELM. Swenson et al. (2019) introduced hillslope
77 hydrology in CLM5 where each grid cell is decomposed into one or more multicolumn hillslopes.
78 The second class of method to account for land surface heterogeneity is called the "continuous
79 approach" in which subgrid heterogeneity is described via analytical or empirical probability
80 density functions (PDFs) instead of dividing a grid cell into subgrid units. For example, He et al.
81 (2021) developed the Fokker-Planck Equation subgrid snow model in the Rapid Update Cycle
82 Land-Surface Model, which uses dynamic PDFs to represent the variability of snow in each grid
83 cell. The third class of method to better account for land surface heterogeneity is by developing
84 parameterizations for subgrid processes. For example, Hao et al. (2021) implemented a sub-grid
85 topographic parameterization in the ELM to represent topographic effects on insolation, including
86 the shadow effects and multi-scattering between adjacent terrains. Besides these three classes of
87 approach dealing with subgrid heterogeneity, the fourth class is to directly increase the grid
88 resolution. Previous studies have demonstrated the benefits of increasing resolution in simulating
89 precipitation, temperature, and related extreme events over multiple spatial scales (Torma et al.,
90 2015; Lindstedt et al., 2015; Cuesta-Valero et al., 2020; Koster et al., 2002; Vegas-Cañas et al.,
91 2020; Rummukainen, 2016). The proposed hyperresolution land surface modeling by Wood et al.
92 (2011) to model land surface processes at a horizontal resolution of 1 km globally and 100 m or
93 finer continentally or regionally has been gaining attention as supported by increasing availability
94 of [high-performance](#) computing resources (Singh et al., 2015; Rouf et al., 2021; Ko et al., 2019;
95 Xue et al., 2021; Yuan et al., 2018; Chaney et al., 2016; Naz et al., 2018; Vergopolan et al., 2020;
96 Garnaud et al., 2016; Bierkens et al., 2014).

97

98 **There are several heterogeneity sources in LSMs but their impact on water and energy**
99 **simulations at different spatial resolutions has not been systematically examined.** Four types
100 of heterogeneity sources are commonly categorized in land surface modeling, including
101 atmospheric forcing, soil properties, land use and land cover, and topography characteristics
102 (Singh et al., 2015; Ji et al., 2017). Singh et al. (2015) showed that including more detailed
103 heterogeneity of soil and topography at high resolutions improved the water and energy
104 simulations over the Southwestern U.S. Xue et al. (2021) demonstrated that simulations over the
105 High Mountain Asia region driven by high-resolution atmospheric forcing generally outperform
106 simulations that used coarse-resolution atmospheric forcing. Simon et al. (2020) investigated the
107 impacts of different heterogeneity sources (e.g., river routing and subsurface flow, soil type, land
108 cover, and forcing meteorology) on coupled simulations using the Weather Research and
109 Forecasting (WRF) model. They found that heterogeneous meteorology is the primary driver for
110 the simulations of energy fluxes, cloud production, and turbulent kinetic energy. Chaney et al.
111 (2016) conducted high-resolution simulations over a humid watershed and found that topography
112 and soils are the main drivers of spatial heterogeneity of soil moisture. However, these studies
113 generally focused either solely on one or a few heterogeneity sources, or were conducted over
114 small domains with limited climate and hydrologic variations. Therefore, a comprehensive
115 assessment of the contribution of different heterogeneity sources to heterogeneity in energy and
116 water fluxes simulated by LSMs at continental scales is needed.

Deleted: of heterogeneity

Deleted: land surface models

117

118 **The relative importance of heterogeneity sources on LSM simulations can be quantified by**
119 **sensitivity analysis (SA), which has been commonly used to study parametric uncertainty**

122 (Saltelli, 2002). In a quantitative sensitivity analysis, the assessed factors could include model
123 parameters as well as any other types of uncertainty induced by varying the input data (Saltelli et
124 al., 2019). The Sobol' SA is a variance-based SA approach and has been widely utilized by the
125 land surface modeling community (Rosolem et al., 2012; Nossent et al., 2011; Li et al., 2013b).
126 The most common application is the assessment of model parameters importance. Cuntz et al.
127 (2016) comprehensively assessed the sensitivities of the Noah-MP land surface model to selected
128 parameters over 12 U.S. basins. This method is also utilized to quantify the sensitivity of model
129 outputs to the choice of parameterization schemes. Dai et al. (2017) proposed a method based on
130 Sobol' variance analysis to conduct SA while simultaneously considering parameterizations and
131 parameters. Zheng et al. (2019) utilized the Sobol' method to quantify the sensitivity of
132 evapotranspiration and runoff to different parameterizations in the Noah-MP land surface model
133 over the CONUS. Given the demonstrated usefulness of the Sobol' sensitivity analysis method, it
134 can be applied to quantify the relative importance of different heterogeneity sources on land
135 surface water and energy simulations.

Deleted: global sensitivity analysis

Deleted: method

Deleted: sensitivity analysis

Deleted: it

136
137 **The overarching goal of this paper is to determine the relative importance of different**
138 **heterogeneity sources on the spatial variability of simulated water and energy partitioning**
139 **over CONUS. The four heterogeneity sources considered in this study are** atmospheric forcing
140 (ATM), soil properties (SOIL), land use and land cover (LULC), and topography (TOPO). Our
141 analysis focuses on their impacts on the water partitioning of precipitation into evapotranspiration
142 and runoff, the energy partitioning of net radiation into sensible heat and latent heat, and their
143 corresponding fluxes. ELMv1 is used as the model testbed. Two sets of experiments are conducted
144 with different combinations of homogeneous and heterogeneous inputs. A set of 16 experiments

Deleted: F

Deleted: are

Deleted: ,

Deleted: including

Deleted: and

154 are used to assess the impacts of the four heterogeneity sources on water and energy partitioning
155 using the Sobol' sensitivity analysis method. Subsequently, another set of 13 experiments are
156 conducted to analyze the heterogeneity effects from each component of atmospheric forcing, soil
157 properties, and topography. The remaining structure of this paper is organized as follows. Section
158 2 describes ELM, data processing, experimental design, and analysis method. Results are
159 examined in section 3, followed by discussions in section 4 and conclusions in section 5.

160 161 **2. Methodology**

162 **2.1 ELM overview**

163 The E3SM is a newly developed state-of-the-science Earth system model by the U.S. Department
164 of Energy (Caldwell et al., 2019; Leung et al., 2020). ELMv1 started from the Community Land
165 Model version 4.5 (CLM4.5; Oleson et al., 2013) and now includes more recently developed
166 representations of soil hydrology and biogeochemistry, riverine water, energy and
167 biogeochemistry, water management (Li et al., 2013a; Tesfa et al., 2014; Bisht et al., 2018; Yang
168 et al., 2019; Zhou et al., 2020).

169 170 **2.2 ELM inputs**

171 **2.2.1 Heterogeneity sources**

172 ATM forcing for ELM consists of seven surface meteorological variables, including precipitation
173 (PRCP), air temperature (TEMP), specific humidity (HUMD), shortwave radiation (SRAD),
174 longwave radiation (LRAD), wind speed (WIND), and air pressure (PRES). Atmospheric forcing
175 from the North American Land Data Assimilation System phase 2 (NLDAS) is used in this study
176 (Xia et al., 2012b, a). SOIL consists of soil texture (STEX), organic matter content (SORG), and
177 soil color (SCOL). STEX and SORG determine soil thermal and hydrologic properties, while

Deleted: Further model developments after the ELMv1 release include subgrid topographic parameterizations for solar radiation (Hao et al., 2021), a subgrid topography structure (Tesfa and Leung, 2017) with subgrid downscaling of atmospheric forcing (Tesfa et al., 2020), and plant hydraulics (Fang et al., 2021). However, these new developments are not included in this study.

187 SCOL regulates the soil albedo and hence surface energy related processes. LULC consists of the
 188 glacier, lake, and urban fractions, the fractional cover of each plant functional type (PFT), and
 189 monthly leaf area index (LAI) and stem area index (SAI) for each PFT. The LULC datasets at
 190 0.05°×0.05° developed by Ke et al. (2012) are used in this study. TOPO consists of the standard
 191 deviation of elevation (SD_ELV), maximum fractional saturated area (Fmax), and topography
 192 slope. TOPO is used in snow cover parameterization, surface runoff generation and infiltration,
 193 SOIL and TOPO datasets are obtained from the NCAR dataset pool for CLM5 (Lawrence et al.,
 194 2019; Lawrence and Chase, 2007; Bonan et al., 2002; Batjes, 2009; Hugelius et al., 2013;
 195 Lawrence and Slater, 2008). Table 1 summarizes these heterogeneity components and resolutions
 196 of the source data. All datasets were prepared over the entire CONUS.

Deleted: The high-resolution datasets of land use land cover, leaf area index, and stem area index

Deleted: for LULC

Deleted: , etc

197 Table 1 Summary of heterogeneity sources in ELM model inputs

Heterogeneity source	Components	Source data resolution
ATM	Precipitation, air temperature, specific humidity, shortwave radiation, longwave radiation, wind speed, air pressure	0.125°, hourly
SOIL	Soil texture, soil organic matter Soil color	0.083°, static 0.5°, static
TOPO	Slope, Standard deviation of elevation, maximum fractional saturated area	0.125°, static
LULC	Fractions of PFTs, wetland, lake, urban characteristics, and glacier <u>LAI for each PFT</u>	0.05°, static 0.05°, monthly

Deleted: Leaf area index (LAI)

199 **2.2.2 Heterogeneous and homogeneous inputs**

200 We prepared heterogeneous and homogeneous inputs at 0.125°×0.125°. The difference between
 201 the two datasets is whether the input values within each 1°×1° region of ELM are spatially
 202 heterogeneous or homogeneous. The SOIL, TOPO, and LULC, were first mapped from their
 203 original resolutions to 0.125°×0.125° resolution, using the Earth System Modeling Framework
 204 (ESMF) regriding tool. Specifically, the first-order conservative interpolation was used for
 205 upsampling dataset (e.g., soil texture), while the nearest neighbor interpolation was used for

Deleted: four

Deleted: types of datasets

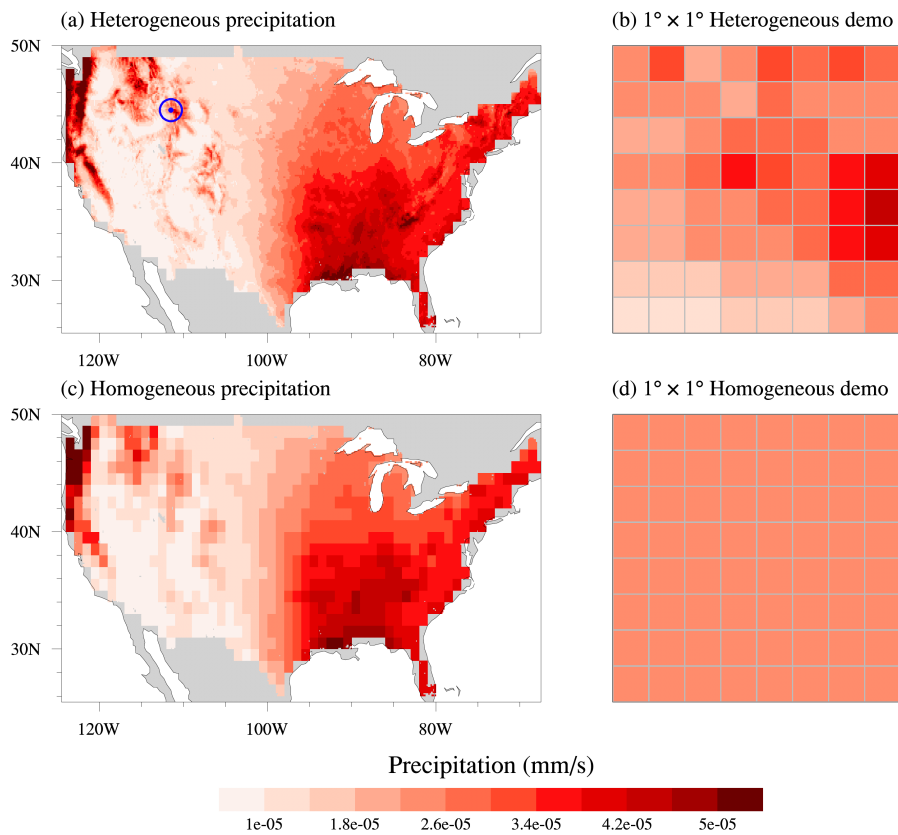
Deleted: listed in Table 1

Deleted: resampled

Deleted: from their original resolutions

216 downscaling dataset (e.g., soil color). These 0.125° resolution datasets are used as the
 217 heterogeneous inputs (Figures 1a and 1b). Then, for each dataset, we replaced the heterogeneous
 218 values of the 64 0.125°×0.125° grids within each 1°×1° region by the mean of the 64 grids (see
 219 Figure 1b vs. 1d). The temporally varying datasets (e.g., hourly ATM and monthly climatology
 220 LAI) were processed at each time interval. As an example, Figure 1 compares the annual
 221 climatology of the heterogeneous and homogeneous precipitation.

Deleted: ,
 Deleted: which



222

225 Figure 1. Annual climatology of (a) heterogeneous and (c) homogeneous precipitation over
 226 CONUS. The corresponding (b) heterogeneous and (d) homogeneous precipitation over a $1^{\circ} \times 1^{\circ}$
 227 region (latitude: $37^{\circ} \text{ N} \sim 38^{\circ} \text{ N}$, longitude: $111^{\circ} \text{ W} \sim 110^{\circ} \text{ W}$, the blue marker in (a)) is also shown.

228

229 2.3 Experimental design and analysis

230 We conducted two sets of ELM experiments over CONUS. The first set contains 16 experiments
 231 with different combinations of heterogeneous and homogeneous inputs from the four heterogeneity
 232 sources (Table 2). These experiments were used to quantify the influence of different heterogeneity
 233 sources on the ELM simulations. The second set of 13 experiments were further conducted to
 234 analyze the impact of heterogeneity from individual components of three heterogeneity sources
 235 (Table 3). As LULC has no explicit individual component, we only analyzed the components of
 236 ATM with seven experiments, SOIL with three experiments, and TOPO with three experiments.
 237 Each experiment only contains one heterogeneous input while other components are homogeneous.
 238 Both the first and second set of experiments were configured at $0.125^{\circ} \times 0.125^{\circ}$ spatial resolution.
 239 The 40-year NLDAS-2 forcing from 1980–2019 was cycled twice to drive the ELM run for 80
 240 years. The first 50-year run was used as model spin-up, and the last 30-year simulation
 241 (corresponding to atmospheric forcing from 1990–2019) was used for further analysis.

242

243 Table 2. The first set of 16 experiments with inputs from ATM, SOIL, LULC, and TOPO.
 244 (0 and 1 denote homogeneous and heterogeneous input from the four heterogeneity sources,
 245 respectively)

No.	Abbr.	ATM	SOIL	LULC	TOPO
EXP1	A0S0L0T0	0	0	0	0
EXP2	A0S0L0T1	0	0	0	1
EXP3	A0S0L1T0	0	0	1	0
EXP4	A0S0L1T1	0	0	1	1
EXP5	A0S1L0T0	0	1	0	0

EXP6	A0S1L0T1	0	1	0	1
EXP7	A0S1L1T0	0	1	1	0
EXP8	A0S1L1T1	0	1	1	1
EXP9	A1S0L0T0	1	0	0	0
EXP10	A1S0L0T1	1	0	0	1
EXP11	A1S0L1T0	1	0	1	0
EXP12	A1S0L1T1	1	0	1	1
EXP13	A1S1L0T0	1	1	0	0
EXP14	A1S1L0T1	1	1	0	1
EXP15	A1S1L1T0	1	1	1	0
EXP16	A1S1L1T1	1	1	1	1

246

247 Table 3. The second set of 13 experiments with inputs from each component of the heterogeneity

248

sources.

No.	Sole heterogeneity input
ATM	
ATM1	Precipitation
ATM2	Air temperature
ATM3	Specific humidity
ATM4	Shortwave radiation
ATM5	Longwave radiation
ATM6	Wind speed
ATM7	Air pressure
SOIL	
SOIL1	Soil texture of sand, silt, and clay
SOIL2	Soil organic matter
SOIL3	Soil color
TOPO	
TOPO1	Fmax
TOPO2	Standard deviation of elevation
TOPO3	Slope

249

250 Our analysis focused on water partitioning, energy partitioning, and related flux variables. The

251 water partitioning is quantified as the ratio between evapotranspiration (ET) and precipitation (P),

252 i.e., ET/P, and the ratio between runoff (R) and precipitation (P), i.e., R/P. The energy partitioning

253 is quantified using the evaporative fraction (EF), which equals the ratio between latent heat (LH)

254 and the sum of latent heat and sensible heat (SH), i.e., $EF = \frac{LH}{LH+SH} * 100 (\%)$. First, the 30-year

Deleted: Based on outputs from each experiment,

256 monthly, seasonal, and annual climatological means were calculated for each experiment at
257 0.125°×0.125° resolution for the five variables of interest (i.e., P, ET, R, LH, and SH). Second, the
258 water and energy partitioning variables (i.e., ET/P, R/P, EF) were computed at 0.125°×0.125°
259 resolution. Third, the standard deviations (SDs) of these variables' climatological mean were
260 calculated for each 1°×1° region from its embedded 64 0.125°×0.125° grids. These 1°×1°
261 resolution SDs of the first and second set of experiments were used in following analysis.
262 For the first set of 16 experiments, we utilized the Sobol' sensitivity analysis to quantify the relative
263 importance of the four heterogeneity sources on water and energy simulations. Detail of Sobol'
264 sensitivity analysis is described in section 2.4.

265 The Sobol' method was not used for the second set of 13 experiments because a comprehensive
266 Sobol' analysis needs 2^{13} experiments, which is computationally infeasible. Instead, the calculated
267 SD of each experiment is used to quantify the impact of heterogeneity of each component, as each
268 experiment only contains one heterogeneous input. Therefore, we compared the SDs between each
269 experiment to determine the relative importance of each component with heterogeneous input
270 (without considering interactions between different components).

272 2.4 The Sobol' sensitivity indices

273 The Sobol' sensitivity analysis (Sobol', 1993) was applied to quantify the sensitivity of spatial
274 variation (i.e., SD) of water and energy partitioning to the four heterogeneity sources based on the
275 first set of 16 experiments. Here, Sobol' first-order sensitivity index measures the direct
276 contribution of a single heterogeneity source to the target variable's spatial variability (e.g., EF's
277 SD). Sobol' higher-order (i.e., second or higher order) sensitivity indices quantify the contribution
278 by the interactions between a given heterogeneity source with other heterogeneity sources. The

Deleted: first

Deleted: ×

Deleted: the

Deleted: encompassed

Deleted: x

Deleted: the

Deleted: total

Deleted: ex

287 sum of all higher-order indices quantifies the overall interaction effects. Sobol' total sensitivity
 288 index measures the total contribution of a given heterogeneity source, which considers both the
 289 first-order and the interaction effects (Zhang et al., 2015; Saltelli et al., 2010). Specifically, the
 290 Sobol' total sensitivity index (ST_{X_i}) and the first-order sensitivity index (S_{X_i}) are given as (Saltelli
 291 et al., 2010),

$$ST_{X_i} = \frac{E_{X_{-i}}(V_{X_i}(Y|X_{-i}))}{V(Y)} \quad (1)$$

$$S_{X_i} = \frac{V_{X_i}(E_{X_{-i}}(Y|X_i))}{V(Y)} \quad (2)$$

294 where X_i is the i -th heterogeneity source (e.g., ATM, SOIL, LULC, and TOPO); X_{-i} denotes the
 295 other heterogeneity sources except X_i ; Y is the SD of a given simulated variable for a given
 296 experiment, and $V(Y)$ is the total variance of the given variable's SDs across all 16 experiments.
 297 Figure 2 illustrates the calculation of Sobol' total and first-order sensitivity indices for LULC (i.e.,
 298 $X_i = LULC$) as follows:

299 (1) For the calculation of ST_{X_i} : First, following Zheng et al. (2019), the SDs of the 16 experiments
 300 are reformed into 8 subgroups based on experiments with different combinations of X_{-i} .
 301 Second, the variance of SD for each subgroup is computed. Third, the mean of SD variances
 302 across 8 subgroups is computed. Fourth, ST_{X_i} is calculated using equation (1).

303 (2) For the calculation of S_{X_i} : First, the SDs of the 16 experiments are reformed into 2 subgroups
 304 based on the experiments either with heterogeneous or homogeneous X_i . Second, the mean of
 305 SDs for each subgroup is computed. Third, the variance of mean SD across 2 subgroups is
 306 calculated. Fourth, S_{X_i} is computed using equation (2).

307 The Sobol' sensitivity indices for ATM, TOPO, and SOIL can be computed similarly.

Deleted: The Sobol' total sensitivity index, , is given as,

319 The corresponding fraction of first-order index ($f_{S_{X_i}}$) and interaction effect index ($f_{SI_{X_i}}$)
320 contributing to the total sensitivity index for X_i can be given as,

321
$$f_{S_{X_i}} = \frac{S_{X_i}}{ST_{X_i}} \times 100 \quad (4)$$

322
$$f_{SI_{X_i}} = 100 - f_{S_{X_i}} \quad (5)$$

323 A more detailed demonstration for the calculation of Sobol' total sensitivity index, first-order
324 sensitivity index, and the interaction effect index is presented in Appendix A. In this paper, the
325 Sobol' total sensitivity index is mainly contributed by Sobol' first-order sensitivity index (see
326 details in section 3.1). Therefore, to make this paper concise, our analysis is based chiefly on Sobol'
327 total sensitivity index if not explicitly pointed out otherwise.

328

329 **2.5 ERA5-Land reanalysis dataset**

330 We further compared the first set of experiments with ERA5-land reanalysis (the land component
331 of the fifth generation of European Centre of Medium-range Weather Forecast reanalysis) (Muñoz-
332 Sabater et al., 2021) to demonstrate the added value in ELM simulations with consideration of
333 heterogeneity sources. ERA5-Land provides a consistent view of terrestrial water and energy
334 cycles at high spatial and temporal resolutions. The monthly ERA5-Land data at $0.1^\circ \times 0.1^\circ$
335 resolution was used in this study. First, the monthly data was regridded using the ESMF regridding
336 tool via the first-order conservative interpolation to $0.125^\circ \times 0.125^\circ$ resolution, which is consistent
337 with the resolution of our sensitivity experiments. Second, the annual and seasonal climatological
338 means for related variables (e.g., ET, R, SH) were computed. Third, SD for each variable was
339 calculated within each $1^\circ \times 1^\circ$ region for further comparisons with the ELM simulations.

340

Deleted: resampled

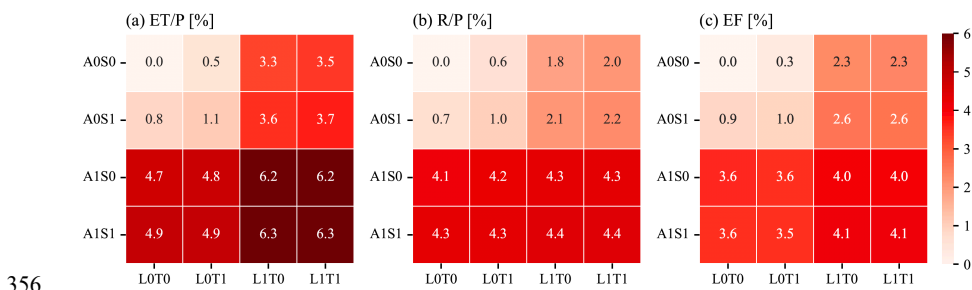
342 **3. Results**

343 **3.1. CONUS overall heterogeneity sensitivities**

344 The inclusion of more heterogeneity sources leads to larger spatial variability in the simulated
 345 ET/P, R/P, and EF (Figure 3). For example, comparing experiment A0S0L0T0 with A1S0L0T0
 346 that includes the ATM heterogeneity, the CONUS averaged SD for ET/P increases from 0 to 4.7%
 347 (Figure 3a). By further comparing experiments in the first and third rows with the second and
 348 fourth rows, ATM always increases the spatial variability of water and energy partitioning.
 349 Similarly, LULC heterogeneity also shows large impacts on the spatial variability for the
 350 partitioning variables as indicated by comparing experiments in the first and third columns with
 351 the second and fourth columns. However, heterogeneity in SOIL and TOPO show negligible
 352 impact. The effects of the heterogeneity sources on the spatial variability of water and energy
 353 partitioning are mainly located in western and central CONUS (Figure S1), which is consistent
 354 with the spatial variability of the heterogeneity inputs, for variables such as precipitation, air
 355 temperature, and longwave radiation (Figure S2).

Deleted: Figure 2

Deleted: Figure 2



356

357 **Figure 3.** CONUS averaged SD of the annual climatology of (a) ET/P, (b) R/P, and (c) EF.

Deleted: Figure 2

358 Combining the X-axis label for LULC and TOPO and the Y-axis label for ATM and SOIL
 359 indicates the names of the experiments listed in Table 2, highlighting the use of heterogeneous
 360 (1) and homogeneous (0) inputs for each heterogeneity source.

364 ATM, with the largest Sobol' total sensitivity index, is the most important heterogeneity source to
365 determine the spatial variability of water and energy partitioning (ET/P, R/P, EF in Figure 4a).
366 LULC is the second most important heterogeneity source (Figure 4a). Even though ATM
367 dominates the spatial heterogeneity of total ET, LULC is the main contributor to the spatial
368 variability of the ET components of transpiration, canopy evaporation, and ground evaporation.
369 The first-order sensitivity indices show similar patterns as the total sensitivity indices (Figure 4b
370 vs. Figure 4a). For the ATM and LULC, their first-order sensitivity indices contribute more than
371 60% of the total sensitivity indices in determining the spatial variability of water and energy
372 partitioning (ET/P, R/P, EF in Figure 4c). Therefore, the total heterogeneity effects of ATM or
373 LULC are mainly due to their own heterogeneity rather than their interactions with other
374 heterogeneity sources. The small proportion of the rest of the total heterogeneity effects of ATM
375 and LULC is contributed by their interactions with other heterogeneity sources (Figure S3b).
376 The heterogeneity of SOIL and TOPO marginally contributes to the spatial variability of water
377 and energy partitioning (Figure 4a). Their effects contributed from their own heterogeneity and
378 their interactions with other heterogeneity sources are relatively small (Figures 4b and S3a). TOPO
379 shows larger impacts on the spatial variabilities of the runoff components than the total runoff
380 (Figure 4a). TOPO's impact on the total runoff is mainly due to its interaction effects with other
381 heterogeneity sources, but its impacts on surface and subsurface runoff are primarily contributed
382 by its own heterogeneity (Figure 4c).
383 Generally, high values of total sensitivity indices are mostly contributed by the first-order
384 sensitivity index (Figures 4a, 4b, and Figure S5). Since our main goal is to analyze the major
385 heterogeneity sources with a large Sobol' total sensitivity index, the results presented in the
386 subsequent sections are based chiefly on Sobol' total sensitivity index.

Deleted: Figure 3

Moved down [2]: However, the heterogeneity of SOIL and TOPO marginally contribute to the spatial variability of water and energy partitioning.

Moved down [1]: TOPO shows larger impacts on the spatial variabilities of the runoff components than the total runoff.

Moved (insertion) [2]

Deleted: However, t

Moved (insertion) [1]

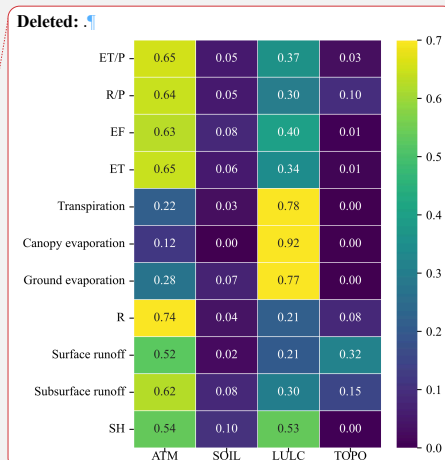
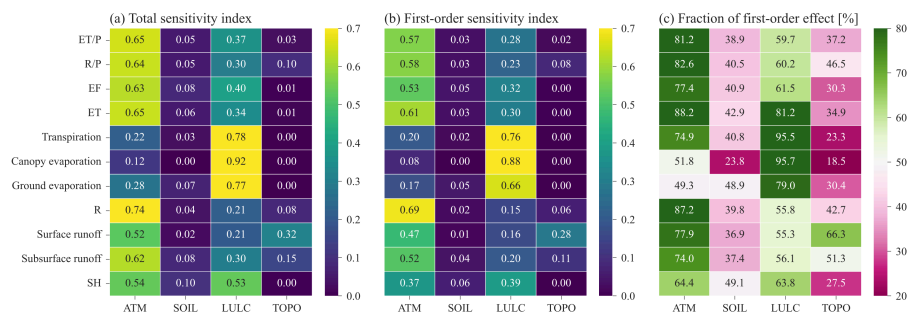


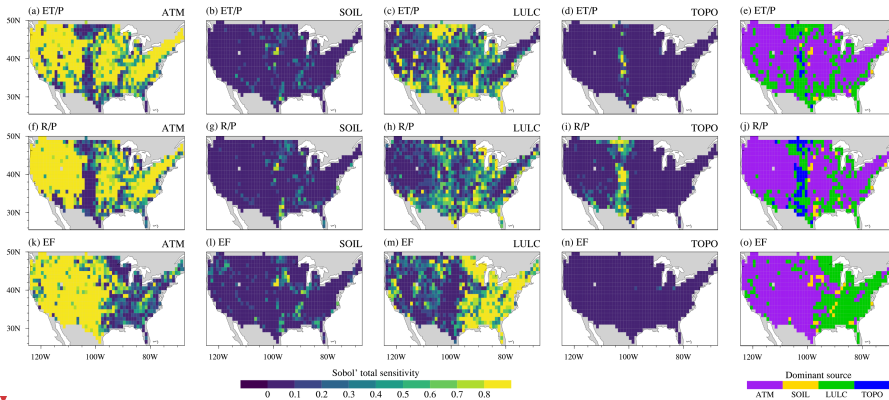
Figure 4. CONUS averaged (a) Sobol' total sensitivity index, (b) Sobol' first-order sensitivity index, and (c) the fraction of first-order effect for the sensitivity of spatial variability of different variables (rows) to the four heterogeneity sources (columns).

3.2 Spatial patterns of heterogeneity sensitivities

The sensitivity of the four heterogeneity sources shows different spatial patterns over CONUS (Figure 5). The water partitioning components, ET/P and R/P, exhibit similar spatial patterns of Sobol' sensitivity index for any given heterogeneity source (Figures 5a-d, 4f-i). ATM shows high Sobol' sensitivity index over most CONUS regions for water and energy partitioning. It dominates the spatial variability of ET/P and R/P over eastern and western CONUS but not central CONUS (Figures 5e and 5j). For the spatial variability of EF, ATM mostly shows dominant effects over central and western CONUS (Figures 5o). LULC is the second most dominant heterogeneity source and dominates most regions over eastern CONUS, although LULC also dominates smaller regions for the spatial variability of ET/P and R/P over central and southeastern CONUS (Figures 5e and 5j). Overall, ATM Sobol' total sensitivity index has opposite spatial patterns compared to LULC Sobol' total sensitivity index (Figure B1 in Appendix B). Therefore, ATM and LULC show complementary contributions to the spatial variability of water and energy partitioning across CONUS. Although TOPO overall has low Sobol' index, it dominates the spatial variability of R/P

- Deleted: Figure 3
- Deleted: Sobol'
- Deleted: sensitivity
- Deleted:
- Deleted: Figure 4
- Deleted: Figures 4
- Deleted: Figures 4
- Deleted: (Figure 4o)
- Deleted: Figures 4
- Deleted: 4

427 over central CONUS (Figure 5j). SOIL has negligible impacts over most regions of CONUS for
 428 the spatial variability of both water and energy partitioning. The spatial distributions of Sobol'
 429 first-order sensitivity indices for the four heterogeneity sources are similar to the Sobol' total
 430 sensitivity indices (Figure 5 vs. Figure S4). First-order sensitivity indices contribute dominantly
 431 to the total sensitivity indices (Figure S5). Therefore, most of the heterogeneity effects on water
 432 and energy partitioning by each heterogeneity source come from its own heterogeneity, with small
 433 proportions from its interaction effects with other heterogeneity sources.



434 **Figure 5.** Spatial patterns of Sobol' total sensitivity index for the four heterogeneity sources
 435 (column 1-4) and the corresponding dominant sources (column 5) for the spatial variability of
 436 water (ET/P and R/P) and energy (EF) partitioning.

438 **3.3 Seasonal variation of heterogeneity sensitivities**

440 The impacts of ATM and LULC on the spatial variability of water and energy fluxes show more
 441 seasonal variations than the impacts of SOIL and TOPO (Figure 6, SOIL and TOPO are not shown
 442 here). This is because ATM and LULC consist of time-varying inputs to the ELM simulations, but

Deleted: Figure 4

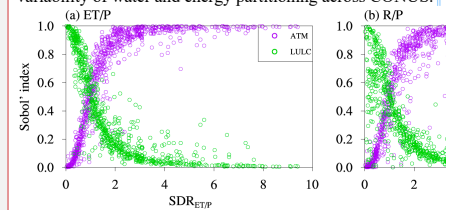
Deleted: ¶

Deleted: Figure 4

Deleted: to

Deleted: ¶

To further explain the spatial patterns of the Sobol' index for the two most dominant heterogeneity sources of ATM and LULC, we further analyzed EXP9 (A1SOL0T0) and EXP3 (A0SOL1T0) listed in Table 2. EXP9 and EXP3 only include heterogeneous inputs from ATM and LULC, respectively. Let us consider ET/P as the quantity of interest for the following discussion. First, the SD of ET/P is computed from the annual climatology (see section 2.3). Next, the SD ratio of ET/P, denoted as $SDR_{ET/P}$, is computed as the ratio between the SD of ET/P in EXP9 and EXP3. $SDR_{ET/P}$ represents the relative spatial variability induced by ATM compared to LULC (Figure S3a). The spatial pattern of the ATM Sobol' index for the ET/P spatial variability shows a positive relationship with the spatial pattern of $SDR_{ET/P}$ (purple circles in Figure 5a, corresponding to Figure 4a vs. Figure S3a). Therefore, a higher value of $SDR_{ET/P}$ indicates that relative to LULC, ATM induces larger ET/P spatial variability, and hence has a higher ATM Sobol' index. Similarly, a lower value of $SDR_{ET/P}$ indicates LULC induces larger ET/P spatial variability than ATM, and hence has a higher LULC Sobol' index (green circles in Figure 5a). Similarly, $SDR_{R/P}$ and SDR_{EF} were calculated for R/P and EF, and they also show a positive (negative) relationship with the corresponding ATM (LULC) Sobol' index (Figures 5b and 5c, and Figures S3b and S3c). We can also see that the ATM Sobol' index has opposite spatial patterns compared to that of the LULC Sobol' index. Therefore, ATM and LULC show complementary contributions to the spatial variability of water and energy partitioning across CONUS. ¶

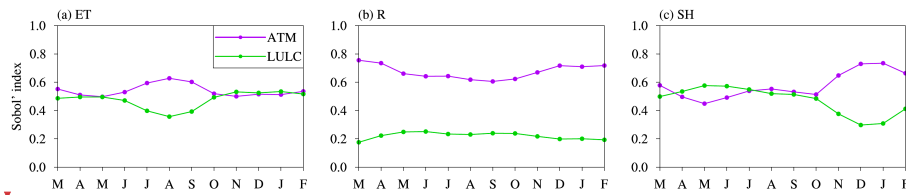


439 **Figure 5.** CONUS spatial relationship between the ATM and LULC Sobol' sensitivity index and the SD ratio for (a) ET/P, (b) R/P, (c) EF. The y-axis values correspond to the spatial patterns of the Sobol' index for ATM (purple) and LULC (green) in Figure 4 (i.e., each circle corresponds to each $1^\circ \times 1^\circ$ region in Figure 4). The x-axis corresponds to the spatial pattern of the SD ratio in Figure S3. ¶

Deleted: Figure

Deleted: 6

487 SOIL and TOPO are time-invariant inputs. Even though the spatial distribution of LULC is
 488 temporally static, the monthly variations in LAI and SAI of different land cover types could affect
 489 the seasonal variation of sensitivity. The heterogeneity impacts of ATM and LULC on the spatial
 490 variability of water and energy fluxes show complementary seasonal variations. The effect of
 491 ATM on the ET spatial variability is larger in July–September than in other months (Figure 6a),
 492 while LULC shows smaller Sobol' index in July–September. The sensitivity of transpiration and
 493 canopy evaporation shows the same seasonal variations (Figures C1d–f in Appendix C). The
 494 spatial variability of R is more sensitive to ATM in the cold season (December–April, Figure 6b),
 495 especially for its component of surface runoff (Figure C1g). The sensitivity of SH spatial
 496 variability to ATM is larger in the non-growing season (i.e., November–March) than in the
 497 growing season (i.e., April–October), with the LULC Sobol' index showing opposite seasonal
 498 variations (Figure 6c).



499
 500 **Figure 6.** Monthly variations of CONUS averaged ATM and LULC Sobol' index for (a) ET, (b)
 501 R, and (c) SH.

502
 503 The spatial patterns of dominant regions by the four heterogeneity sources vary over different
 504 seasons. Compared with spring and winter, ATM dominates the ET spatial variability in more
 505 regions than in summer and fall when ATM is more dominant over eastern CONUS (Table 5 and
 506 Figures S6a–d). LULC shows opposite seasonal spatial patterns with more dominant regions in

Deleted: Figure 6a

Deleted: S4a

Deleted: c

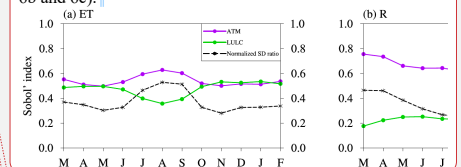
Deleted: Figure 6

Deleted: S4d

Deleted: ¶

Deleted: ¶

To further explain the seasonal variations of the Sobol' index for ATM and LULC, the SD of ET for each month was calculated as an example from monthly mean climatology and the SD ratio for each month was computed as the ratio between the SD of ET in EXP9 and EXP3. For each $1^\circ \times 1^\circ$ region, the 12 monthly SD ratios were normalized to [0, 1] using minimum and maximum values. Finally, the CONUS average of the normalized SD ratios was computed for each month, denoted as $NSDR_{ET}$. A higher value of $NSDR_{ET}$ denotes ATM induces more ET spatial variability than LULC. Therefore, $NSDR_{ET}$ shows similar seasonal variations with the ATM Sobol' index for ET spatial variability (black curve vs. purple curve in Figure 6a), but opposite seasonal variations with the LULC Sobol' index (black curve vs. green curve in Figure 6a). Similarly, $NSDR_R$ and $NSDR_{SH}$ were calculated for R and SH, and they also show a similar (opposite) seasonal variation with the corresponding seasonal ATM (LULC) Sobol' index (Figures 6b and 6c).



Deleted: Figure

Deleted: 6

Deleted: and normalized SD ratio

Deleted: S5

538 eastern CONUS over spring and winter. As for the R spatial variability, TOPO shows large spatial
 539 variation of its dominant regions over different seasons (Figures S6f~i). Besides its dominant
 540 contribution in central CONUS over all seasons, TOPO also dominates the R spatial variability in
 541 parts of eastern US in the summer and autumn (Figures S6g~h). For the EF spatial variability,
 542 ATM has more contributions in the fall and winter but smaller contributions in spring and summer
 543 than LULC (Table 5). LULC shows more dominant regions over eastern CONUS, especially in
 544 spring and summer (Figures S6k~i). To understand the seasonal variations of dominant
 545 heterogeneity sources, the seasonal variations of Sobol' total sensitivity index and induced R's SD
 546 are demonstrated at one gridcell over eastern US (Figure S7). Compared with other heterogeneity
 547 sources, ATM induced R's SD shows an apparent seasonal variation, with high values in spring
 548 and winter but small values in summer and fall (Figure S7b). Therefore, ATM is the dominant
 549 heterogeneity source in spring and winter. Even though TOPO and SOIL induced R's SDs show
 550 slight seasonal variations (Figure S7), they dominate R's spatial variability in summer and fall,
 551 respectively.

Deleted: S5

Deleted: S5

Deleted: S5

552 Table 5 Grid percentage of the dominant heterogeneity source in determining the spatial
 553 variability of ET, R, and SH for four seasons and annual mean (ANN)

Deleted: ¶

Seasons	ATM	SOIL	LULC	TOPO
ET				
Spring (MAM)	51	4	46	0
Summer (JJA)	63	3	34	0
Fall (SON)	57	2	42	0
Winter (DJF)	49	0	51	0
ANN	66	2	31	0
R				
Spring (MAM)	81	2	13	5
Summer (JJA)	67	4	17	11
Fall (SON)	66	6	18	11
Winter (DJF)	75	2	12	10
ANN	77	1	15	7
SH				
Spring (MAM)	44	5	51	0
Summer (JJA)	45	2	53	0
Fall (SON)	52	5	44	0

Winter (DJF)	69	2	29	0
ANN	49	4	47	0

558

559 3.4 Effects of ATM heterogeneity components

560 Based on the second set of 13 experiments, we analyzed the heterogeneity effects by each
561 component of ATM, SOIL, and TOPO (Figure 7), respectively. Precipitation is the largest ATM
562 heterogeneity source in determining the spatial variability of water fluxes (Figures 7a~b),
563 especially over western and central CONUS for ET (Figure 7a) and almost the entire CONUS for
564 R (Figure 7b). Air temperature dominates the spatial variability of ET in eastern CONUS (Figure
565 7a). The spatial variability of SH is mainly dominated by the incoming longwave radiation in
566 western CONUS and by the air temperature in eastern CONUS (Figure 7c). Longwave radiation
567 provides more energy input and contributes more to the SH spatial variability than shortwave
568 radiation (Figure 8c). Among the SOIL components, soil texture, which can influence soil moisture
569 and runoff generation, shows the largest effects on the ET and R spatial variability over most
570 CONUS regions (Figures 7d, 7e, 8d, and 8e). Soil color, affecting the surface albedo and energy
571 balance, shows the largest impacts on the SH spatial variability over central CONUS (Figures 7f
572 and 8f). Fmax is the most essential TOPO component, offering the largest effects on the spatial
573 variability of ET, R, and SH over most CONUS regions (Figures 7g~i and Figures 8g~i). Fmax
574 regulates surface runoff generation and infiltration, and therefore influences the soil moisture, ET,
575 and SH. SD_ELV and slope can affect surface water and snow cover fraction, and consequently,
576 they show the largest impacts over northwestern CONUS regions with mountains and snowpack.

Deleted: Figure

Deleted: 7

Deleted: Figures S6a

Deleted: Figure

Deleted: 7

Deleted: Figure

Deleted: 7

Deleted: Figure

Deleted: 7

Deleted: Figure 7c

Deleted: Figure S6

Deleted: Figures 7

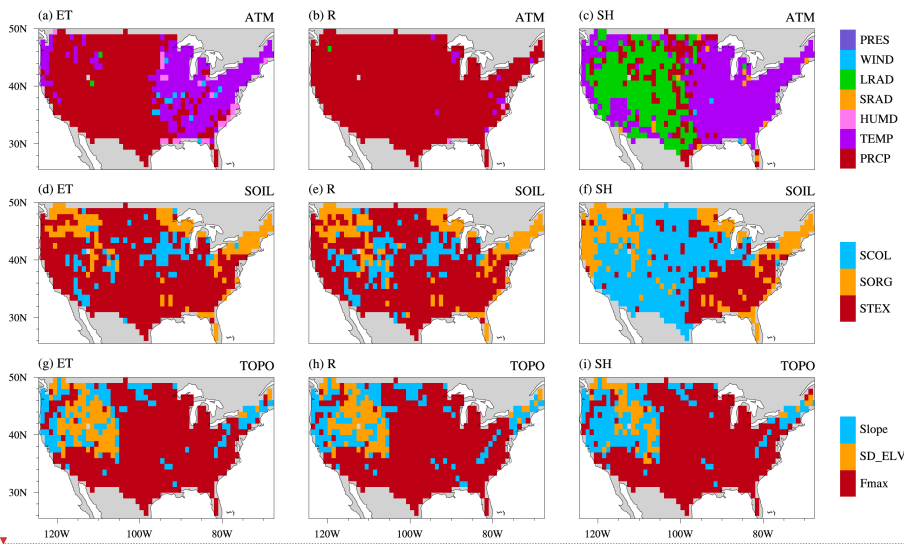
Deleted: and

Deleted: 7

Deleted: Figures 7

Deleted: Figures 7

Deleted: Figures S6



Deleted: The spatial variability induced by all components (of ATM, SOIL, or TOPO) is larger than that induced by each individual component. However, it is smaller than the sum of the spatial variability induced by each component (Figure S6). For example, the CONUS averaged SD for ET caused by all SOIL components is $1.9 (10^{-7} \text{ mm/s})$, which is smaller than $2.5 (10^{-7} \text{ mm/s})$, the sum of the SD of ET induced by STEX, SORG, and SCOL (Figure S6d). Therefore, the additional SD induced by an additional heterogeneity component decreases, suggesting that the effect of heterogeneity on the spatial variability of water and energy fluxes saturates, possibly due to interactions among the processes influenced by the heterogeneity sources.

594
 595 **Figure 7.** The largest induced spatial variability for the annual climatological mean of ET (left
 596 column), R (middle column), and SH (right column) induced by each component of ATM (top
 597 panel), SOIL (middle panel), and TOPO (bottom panel)

Deleted: Figure

Deleted: 7

Formatted: Line spacing: Double

598
 599 The spatial variability induced by all components (of ATM, SOIL, or TOPO) is larger than that
 600 induced by each individual component. However, it is smaller than the sum of the spatial
 601 variability induced by each component (Figure 8). For example, the CONUS averaged SD for ET
 602 caused by all SOIL components is $1.9 (10^{-7} \text{ mm/s})$, which is smaller than $2.5 (10^{-7} \text{ mm/s})$, the sum
 603 of the SD of ET induced by STEX, SORG, and SCOL (Figure 8d). Therefore, the additional SD
 604 induced by an additional heterogeneity component decreases, suggesting that the effect of
 605 heterogeneity on the spatial variability of water and energy fluxes saturates, due to the interaction
 606 effects between heterogeneity components on related water and energy processes,

Deleted: Figure

Deleted: 7

Deleted: Figure

Deleted: 7

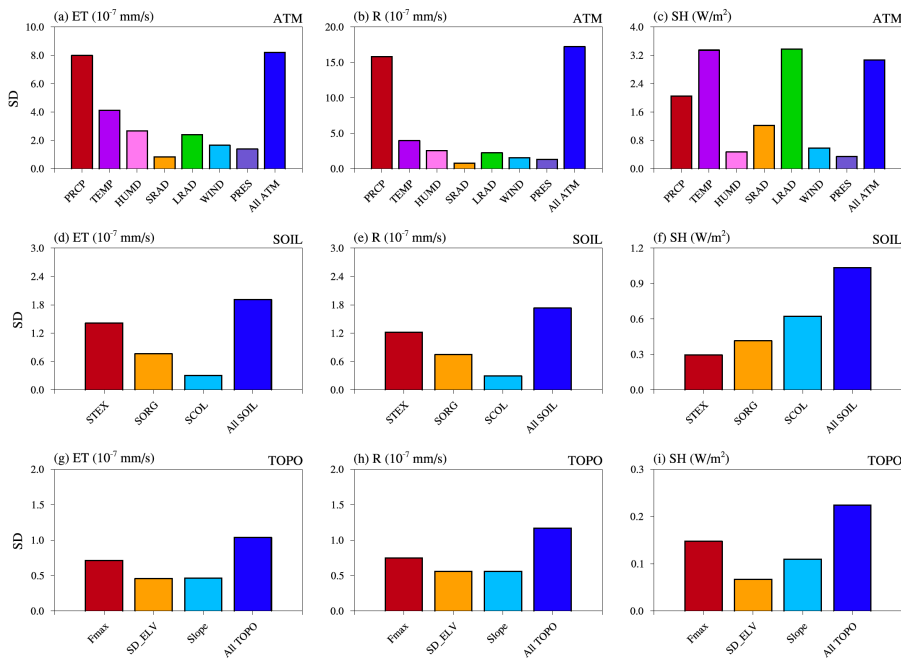
Deleted: possibly

Deleted: effects

Deleted: among

Deleted: the

Deleted: influenced by the heterogeneity sources



631

632

633

634

635

636

3.5 Comparison with ERA5-Land reanalysis

637

Higher consistency of the spatial variability between the simulations and ERA5-Land reanalysis

638

(i.e., smaller SD difference) is obtained when more sources of heterogeneity are accounted for in

639

the simulations for ET, R, and SH (Figure 9). ATM and LULC dominate the improvements in the

640

spatial variability of model simulations. Generally, ATM heterogeneity leads to more or similar

641

improvements than LULC heterogeneity for ET, R, and SH over all seasons. For example, in

642

Figure 9a, ATM induced larger improvements, as shown by comparing experiments in the first

Deleted: Figure 7

Deleted: or

Deleted: Figure

Deleted: 8

Deleted: of

Deleted: Figure

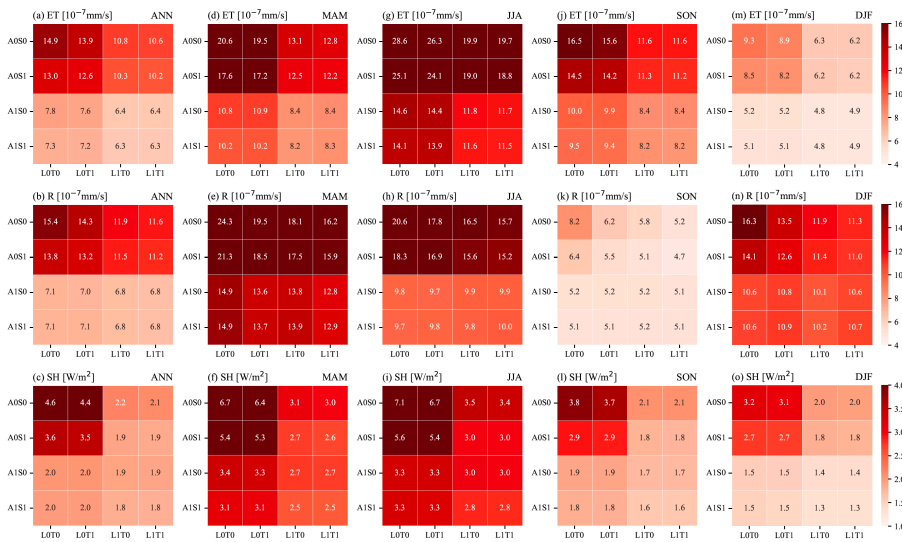
Deleted: 8

650 and third rows with the second and fourth rows, than the LULC induced improvements, comparing
651 experiments in the first and third columns with the second and fourth columns. The SD difference
652 is usually larger over MAM and JJA than SON and DJF, probably due to the heterogeneity
653 difference between the NLDAS and ERA5 atmosphere forcing as ATM is the major heterogeneity
654 contributor.

655 Improvements of the spatial variability of model simulations are primarily distributed over western
656 and eastern CONUS for ET, R, and SH (e.g., Figures S8 and S9, 1st column vs. 4th column). Overall,
657 the ELM simulated ET and SH have smaller SDs than those of ERA5 Land (Figures S9d and S9f).
658 Meanwhile the simulated R has larger SD especially in the western US than that of ERA5 Land,
659 probably mainly due to ATM's heterogeneity effects (Figures S9e vs. S9g). For ET and R, ATM
660 mainly increases their spatial variability over western and eastern CONUS (Figures S8a vs. S8c,
661 and S8e vs. S8g), and LULC mostly shows changes over eastern CONUS (Figures S8a vs. S8b,
662 and S8e vs. S8f). Both ATM and LULC increase SH spatial variability over western and eastern
663 CONUS (Figure S8i vs. S8j, and S8j vs. S8k).

Deleted:
Deleted: and R, and western CONUS for
Deleted: S
Deleted: 7

Deleted: improves
Deleted: S
Deleted: 7
Deleted: S7c
Deleted: S7e
Deleted: S7g
Deleted: improvements
Deleted: S
Deleted: 7
Deleted: S7b
Deleted: S7e
Deleted: S7f
Deleted: show improvements in the
Deleted: Figure S7
Deleted: S
Deleted: 7
Deleted: S
Deleted: 7
Deleted: S
Deleted: 7



688

689 **Figure 9.** CONUS averaged absolute difference of SD between 16 ELM experiments and ERA5-
 690 Land reanalysis for the annual (1st column) and seasonal (2nd – 5th column) climatological mean
 691 of ET (top panel), R (middle panel), and SH (bottom panel).

692

693 **4. Discussions**

694 ATM and LULC are the two most essential heterogeneity sources contributing to the spatial
 695 variability of water and energy partitioning. Their total heterogeneity effects are mostly
 696 contributed by their own heterogeneity, with small proportions are contributed by their interactions
 697 with other heterogeneity sources. Simon et al. (2020) also found that the heterogeneous
 698 meteorological forcing is the primary driver for the spatial variability of latent heat and sensible
 699 heat in WRF simulations. The Sobol' sensitivity index averaged over the same region (a 100 km ×
 700 100 km domain centered at 36.6° N, 97.5° W) as Simon et al. (2020) also indicates that ATM is
 701 the dominant heterogeneity source. Therefore, better representation of ATM heterogeneity in

Deleted: Figure 8

Deleted: Our results are consistent with
 Deleted: , who

705 climate models is crucial for modeling the water and energy partitioning, especially for the three
706 major components of precipitation, air temperature, and longwave radiation. Tesfa et al. (2020)
707 compared several simple approaches to capturing ATM heterogeneity for downscaling the grid
708 mean precipitation to topography-based subgrids for land surface modeling. Besides ATM, LULC
709 is the second most crucial heterogeneity source. Notably, anthropogenic land use and land cover
710 change has been shown to have large impacts on land-atmosphere interaction, land surface
711 hydrology, and associated extreme events (Findell et al., 2017; Li et al., 2018, 2015; Swann et al.,
712 2010; Zeng et al., 2017; Yuan et al., 2021; PIELKE et al., 2007). Therefore, the heterogeneity of
713 LULC should also be well considered in climate modeling.

Deleted: One approach of capturing ATM heterogeneity has been developed by

714

715 ATM and LULC show complementary contributions to the spatial variability of water and energy
716 partitioning spatially over CONUS and temporally in different seasons. Sobol' sensitivity analysis
717 is a standardized quantification of the relative importance of different heterogeneity sources. The
718 sum of the Sobol' indices for the four heterogeneity sources roughly equals one. As the two
719 dominant heterogeneity sources, ATM Sobol index and LULC Sobol' index dominate the sum of
720 all Sobol' indices. Hence, they show complementary patterns spatially (Figure B1) and temporally
721 (Figure 6). In addition, ATM and LULC show complementary contributions across different
722 climate zones. The Budyko's aridity index (BAI, Budyko 1974), which is the ratio of annual net
723 radiation to the product of the latent heat of water vaporization and the annual precipitation, was
724 calculated using the outputs from EXP16. From humid (low BAI) to arid climate (high BAI), a
725 decreasing fraction of the CONUS region is dominated by ATM in determining the ET/P spatial
726 variability (Figure 10a). At the same time, LULC shows an increasing contribution to the ET/P
727 spatial variability with BAI. The spatial variability of energy partitioning exhibits even more

Deleted: indexes

Deleted: indexes

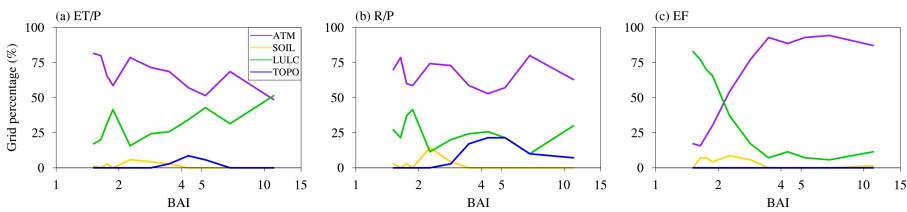
Deleted: 5

Deleted: Figure 6

Deleted: Figure

Deleted: 9

736 complementarity between the ATM and LULC contributions from arid regions to humid regions
 737 (Figure 10c). In more arid regions limited by water, EF spatial variability is much more dominated
 738 by heterogeneity of ATM, likely through the heterogeneous precipitation, but in humid regions
 739 limited by energy, LULC dominates the EF spatial variability through its influence on surface
 740 albedo and surface roughness.



741

742 **Figure 10.** The grid percentage of dominant heterogeneity sources along with Budyko's aridity
 743 index. A higher aridity index means more arid.

744

745 SOIL and TOPO show relatively small impacts on the spatial variability of water and energy
 746 partitioning. However, TOPO has a dominant influence on the R/P spatial variability over the
 747 transitional zone (Figure 10b) of central CONUS located between the arid western CONUS and
 748 the humid eastern CONUS (Figure 5). TOPO's impact on the total runoff is mainly due to its
 749 interaction effects with other heterogeneity sources (Figure 4). SOIL shows some dominant effects
 750 on the spatial variability of water and energy partitioning over a small proportion of humid regions

751 (Figure 10). The heterogeneity in SOIL and TOPO was derived from coarse resolution data at
 752 0.125°×0.125° spatial resolution, which could be a possible reason for the minor SOIL and TOPO
 753 effects. Singh et al. (2015) found that CLM4.0 did not show much improvement when model
 754 resolution increased from ~100 km to ~25 km but improvement was noticeable at finer 1 km

Deleted: Figure
 Deleted: 9

Deleted: Figure
 Deleted: 9

Deleted: Figure
 Deleted: 9
 Deleted: Figure 4

Deleted: orange curve in Figure
 Deleted: 9

764 resolution. Additionally, exclusion of lateral subsurface flow in ELMv1 could also lead to
765 underestimation of the contributions from SOIL and TOPO.

766

767 The current study excluded a few land surface processes that have been included in LSMs in the
768 last decade, limiting our ability to assess the role of land surface heterogeneity in spatiotemporal
769 variability of energy and water partitioning. For example, the hillslope processes of lateral ridge-
770 valley flow and the insolation contrasts between sunny and shady slopes are crucial for land surface
771 modeling (Fan et al., 2019; Taylor et al., 2012; Clark et al., 2015; Scheidegger et al., 2021), but
772 they are neglected in this study. Sean et al. (2019) incorporated the representative hillslope concept
773 into the CLM5, and they found that subgrid hillslope process induced large differences in
774 evapotranspiration between upland and lowland hillslope columns in arid and semiarid regions.
775 Krakauer et al. (2014) suggested that the magnitude of between-grid groundwater flow becomes
776 significant over larger regions at higher model resolution. Xie et al. (2020) also demonstrated the
777 importance of groundwater lateral flow in offsetting depression cones caused by intensive
778 groundwater pumping. Fang et al. (2017) compared the ACME Land Model (the earlier version of
779 ELM) and the three-dimensional ParFlow variably saturated flow model (Maxwell et al., 2015),
780 underscoring ELM limitation in capturing topography's influence on groundwater and runoff.
781 Additionally, topography also significantly influences insolation, including the shadow effects and
782 multi-scattering between adjacent terrain. Hao et al. (2021) implemented a sub-grid topographic
783 parameterization in ELM, which improves the simulated surface energy balance, snow cover, and
784 surface air temperature over the Tibetan Plateau. The inclusion of plant hydraulics has also shown
785 essential improvements in water and carbon simulations under drought conditions (Li et al., 2021;
786 Fang et al., 2021), which should also be considered in future research, especially as vegetation

787 may experience more hydroclimate drought stress in projected future climate conditions (Yuan et
788 al., 2019; Xu et al., 2019; Li et al., 2020). The subgrid downscaling of atmospheric forcing (Tesfa
789 et al., 2020), which could further enhance the representation of heterogeneity effects on water and
790 energy simulations, is also unaccounted for in this study.

791

792 5. Conclusions

793 This study comprehensively investigated the impacts of different heterogeneity sources (i.e., ATM,
794 LULC, SOIL, TOPO) on the spatial variability of water and energy partitioning over CONUS.

795 Two sets of experiments were conducted based on different combinations of spatially
796 heterogeneous and homogeneous datasets. Based on the first set of 16 experiments, Sobol' total

797 ~~and first-order sensitivity indices~~ were utilized to identify the relative importance of the four
798 heterogeneity sources. The second set of 13 experiments were further used to assess the influence

799 from individual components of ATM, SOIL, and TOPO. Our results show that ATM and LULC
800 are the two dominant heterogeneity sources in determining the spatial variability of water and

801 energy partitioning. ~~largely contributed by ATM's or LULC's own heterogeneity and slightly~~
802 ~~contributed by their interactions with other heterogeneity sources~~. Their heterogeneity effects are

803 spatially complementary across CONUS, and temporally complementary across seasons. The
804 complementary contributions of ATM and LULC reflect the overall negligible impacts of SOIL

805 and TOPO, but the complementarity also reflects physically the clear demarcation of climatic
806 zones across CONUS, featuring the arid, water-limited western CONUS dominantly influenced

807 by ATM (precipitation in particular) and the humid, energy-limited eastern CONUS dominantly
808 influenced by LULC. In the transitional climate zone of central CONUS, TOPO shows some

809 dominant influence on the R/P spatial variability. The overall most essential components for ATM

Deleted: sensitivity

Deleted: analysis

812 (precipitation, temperature, and longwave radiation), SOIL (soil texture and soil color), and TOPO
813 (Fmax) were also identified. Comparison with ERA5-Land reanalysis reveals that accounting for
814 more sources of heterogeneity improved the simulated spatial variability of water and energy
815 fluxes, although such improvements tend to saturate as more heterogeneous sources were added.
816 The relative importance of different heterogeneity sources quantified in this study is useful for
817 prioritizing spatial heterogeneity to be included for improving land surface modeling. We note,
818 however, that the present assessment is limited by how well the input datasets capture the
819 spatiotemporal heterogeneity and how well the land surface model ~~represents~~ processes such as
820 hillslope hydrology and topographic effect on solar radiation that are influenced by land surface
821 heterogeneity. This motivates the use of more process-rich models such as distributed or three-
822 dimensional subsurface hydrology models to provide benchmarks of the relative importance of
823 heterogeneity sources to help prioritize future development of land surface models to improve
824 modeling of energy and water fluxes.

825

Deleted: represent

827 **Appendix A: demonstration of Sobol' index calculation**

828 Here we give an example for the calculation of Sobol' total, first-order and interaction effect
 829 indices, ST_{LULC} , S_{LULC} , and SI_{LULC} to quantify the sensitivity of EF's spatial variability to LULC
 830 in a $1^\circ \times 1^\circ$ region at 39.5N and 107.5W.

831 (1) Calculation of ST_{LULC} (Table A1): Following Zheng et al. (2019), and based on equation (1)
 832 and Figure 2, the 16 experiments are grouped into 8 subgroups containing two experiments, where
 833 the difference between the two experiments in a given subgroup is homogeneous vs. heterogeneous
 834 LULC. The SDs of the 16-experiments are listed in C1. The variance of each subgroup is computed
 835 in C2, which represents the influence of LULC heterogeneity. The average impact of LULC
 836 heterogeneity from the eight subgroups in C3 is computed as the mean of the values in C2. The
 837 total variance of these 16 SDs in C1 is computed in C4. Finally, the ratio between C3 and C4 is
 838 calculated as Sobol' total sensitivity index in C5, which quantifies EF spatial variability sensitivity
 839 to LULC heterogeneity.

840 (2) Calculation of S_{LULC} and SI_{LULC} : Similarly, based on the equations (2) and (3) and Figure 2,
 841 we then compute the Sobol' first-order sensitivity index (Table A2) and the Sobol' interaction effect
 842 index (Table A3), and their contribution fractions to the total sensitivity index (Table A3).

843 **Table A1 Calculation of Sobol' total sensitivity index**

Experiments	$Y _{\sim LULC}$	$V_{LULC}(Y _{X_{\sim LULC}})$	$E_{\sim LULC}(V_{LULC}(Y _{X_{\sim LULC}}))$	$V(Y)$	ST_{LULC}
C0	C1	C2	C3	C4	C5
A0S0L0T0	0.00	6.88			
A0S0L1T0	5.24				
A0S0L0T1	0.57	6.28			
A0S0L1T1	5.58				
A0S1L0T0	0.32	6.75			
A0S1L1T0	5.51		3.32	26.99	0.12
A0S1L0T1	0.69	6.64			
A0S1L1T1	5.84				
A1S0L0T0	12.88	0.01			
A1S0L1T0	12.67				
A1S0L0T1	12.80	0.00			

<u>A1S0L1T1</u>	<u>12.76</u>	
<u>A1S1L0T0</u>	<u>12.71</u>	<u>0.01</u>
<u>A1S1L1T0</u>	<u>12.51</u>	
<u>A1S1L0T1</u>	<u>12.63</u>	<u>0.00</u>
<u>A1S1L1T1</u>	<u>12.59</u>	

844

845

Table A2 Calculation of Sobol' first-order sensitivity index

<u>Experiments</u>	<u>$Y LULC$</u>	<u>$E_{-LULC}(Y X_{LULC})$</u>	<u>$V_{LULC}(E_{-LULC}(Y X_{LULC}))$</u>	<u>$V(Y)$</u>	<u>S_{LULC}</u>
<u>C0</u>	<u>C1</u>	<u>C2</u>	<u>C3</u>	<u>C4</u>	<u>C5</u>
<u>A0S0L0T0</u>	<u>0.00</u>				
<u>A0S0L0T1</u>	<u>0.57</u>				
<u>A0S1L0T0</u>	<u>0.32</u>				
<u>A0S1L0T1</u>	<u>0.69</u>				
<u>A1S0L0T0</u>	<u>12.88</u>	<u>6.58</u>			
<u>A1S0L0T1</u>	<u>12.80</u>				
<u>A1S1L0T0</u>	<u>12.71</u>				
<u>A1S1L0T1</u>	<u>12.63</u>				
<u>A0S0L1T0</u>	<u>5.24</u>		<u>1.58</u>	<u>26.99</u>	<u>0.058</u>
<u>A0S0L1T1</u>	<u>5.58</u>				
<u>A0S1L1T0</u>	<u>5.51</u>				
<u>A0S1L1T1</u>	<u>5.84</u>				
<u>A1S0L1T0</u>	<u>12.67</u>	<u>9.09</u>			
<u>A1S0L1T1</u>	<u>12.76</u>				
<u>A1S1L1T0</u>	<u>12.51</u>				
<u>A1S1L1T1</u>	<u>12.59</u>				

846

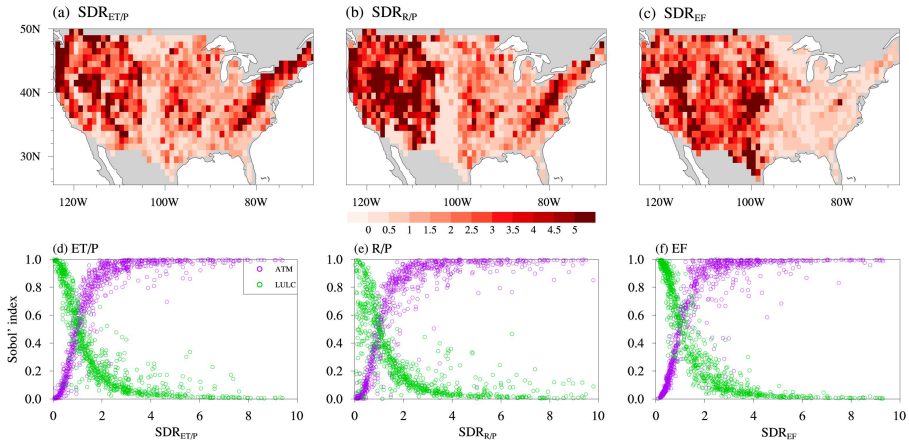
847

Table A3 Calculation of Sobol' interaction effect index and contributing fractions

	<u>ST_{LULC}</u>	<u>S_{LULC}</u>	<u>SI_{LULC}</u>
<u>Index value</u>	<u>0.12</u>	<u>0.058</u>	<u>0.065</u>
<u>Fraction to total</u>		<u>47.5%</u>	<u>52.5%</u>

848

849 **Appendix B: Spatial patterns of Sobol' total sensitivity index vs. SD ratio**
850 To further understand the spatial patterns of the Sobol' total sensitivity index for the two most
851 dominant heterogeneity sources of ATM and LULC (Figure 5), we further analyzed EXP9
852 (A1S0L0T0) and EXP3 (A0S0L1T0) listed in Table 2. EXP9 and EXP3 only include
853 heterogeneous inputs from ATM and LULC, respectively. Let us consider ET/P as the quantity of
854 interest for the following discussion. First, the SD of ET/P is computed from the annual
855 climatology (section 2.3). Next, the SD ratio of ET/P, denoted as $SDR_{ET/P}$, is computed as the
856 ratio between the SD of ET/P in EXP9 and EXP3. $SDR_{ET/P}$ represents the relative spatial
857 variability induced by ATM compared to LULC (Figure B1a). The spatial pattern of the ATM
858 Sobol' total sensitivity index for the ET/P spatial variability shows a positive relationship with the
859 spatial pattern of $SDR_{ET/P}$ (purple circles in Figure B1d, corresponding to Figure 5a vs. Figure
860 B1a). Therefore, a higher value of $SDR_{ET/P}$ indicates that relative to LULC, ATM induces larger
861 ET/P spatial variability, and hence has a higher ATM Sobol' total sensitivity index. Similarly, a
862 lower value of $SDR_{ET/P}$ indicates LULC induces larger ET/P spatial variability than ATM, and
863 hence has a higher LULC Sobol' total sensitivity index (green circles in Figure B1d). Similarly,
864 $SDR_{R/P}$ and SDR_{EF} were calculated for R/P and EF, and they also show a positive (negative)
865 relationship with the corresponding ATM (LULC) Sobol' total sensitivity index (Figures B1b, B1c,
866 B1e, and B1f). We can also see that the ATM Sobol' total sensitivity index has opposite spatial
867 patterns compared to the LULC Sobol' total sensitivity index. Therefore, ATM and LULC show
868 complementary contributions to the spatial variability of water and energy partitioning across
869 CONUS.



870

871

872

873

874

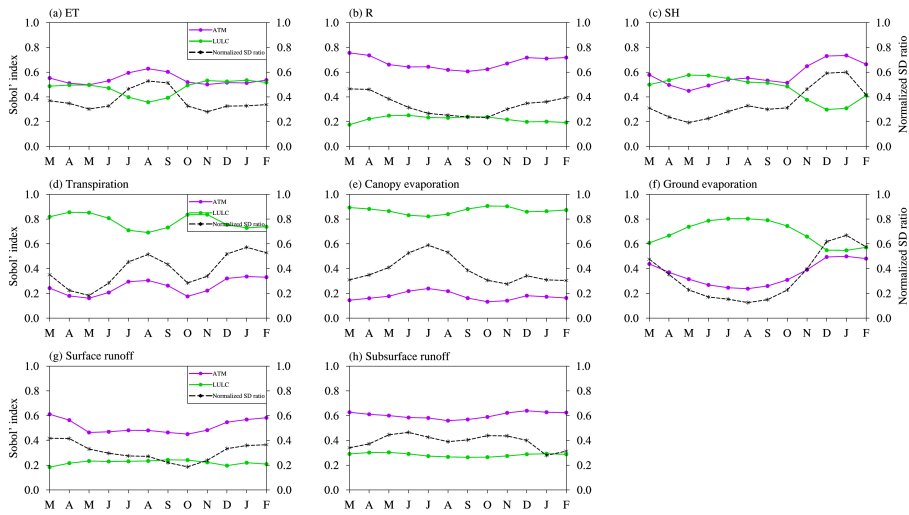
875

876

Figure B1. Spatial patterns of SD ratios (top panel) and their spatial relationship with the ATM and LULC Sobol' total sensitivity index (bottom panel) for ET/P, R/P and EF, respectively. The y-axis values correspond to the spatial patterns of the Sobol' total sensitivity index for ATM (purple) and LULC (green) in Figure 5 (i.e., each circle corresponds to each 1°×1° region).

877 **Appendix C: Seasonal variations of Sobol' total sensitivity index vs. normalized SD ratio**
878 To further explain the seasonal variations of the Sobol' total sensitivity index for ATM and LULC,
879 the SD of ET for each month was calculated as an example from monthly mean climatology. The
880 SD ratio for each month was computed as the ratio between the SD of ET in EXP9 and EXP3. For
881 each $1^{\circ} \times 1^{\circ}$ region, the 12 monthly SD ratios were normalized to [0, 1] using minimum and
882 maximum values. Finally, the CONUS average of the normalized SD ratios was computed for each
883 month, denoted as $NSDR_{ET}$. A higher value of $NSDR_{ET}$ denotes ATM induces more ET spatial
884 variability than LULC. Therefore, $NSDR_{ET}$ shows similar seasonal variations with the ATM
885 Sobol' total sensitivity index for ET spatial variability (black curve vs. purple curve in Figure C1a),
886 but opposite seasonal variations with the LULC Sobol' total sensitivity index (black curve vs. green
887 curve in Figure C1a). Similarly, normalized SD ratios were calculated for R, SH, ET components
888 and R components, and they also show a similar (opposite) seasonal variation with the
889 corresponding seasonal ATM (LULC) Sobol' total sensitivity index (Figures C1).

890



891

892 Figure C1. Monthly variations of CONUS averaged ATM and LULC Sobol' total sensitivity index
 893 to ATM and normalized SD ratio for (a) ET, (b) R, and (c) SH, (d) Transpiration, (e) Canopy
 894 evaporation, (f) Ground evaporation, (g) Surface runoff, and (h) Subsurface runoff, respectively

895

896

897 *Code and Data Availability.* NLDAS-2 forcing is available from
898 <https://ldas.gsfc.nasa.gov/nldas/v2/forcing>. SOIL and TOPO related datasets are downloaded
899 from <https://svn-ccsm-inputdata.cgd.ucar.edu/trunk/inputdata/lnd/clm2/rawdata/>. LULC related
900 datasets are from Ke et al. (2012); ERA5-Land reanalysis is available from:
901 [https://cds.climate.copernicus.eu/cdsapp#!/dataset/reanalysis-era5-land-monthly-](https://cds.climate.copernicus.eu/cdsapp#!/dataset/reanalysis-era5-land-monthly-means?tab=overview)
902 [means?tab=overview](https://cds.climate.copernicus.eu/cdsapp#!/dataset/reanalysis-era5-land-monthly-means?tab=overview). The ELM source code and surface data (e.g., SOIL, TOPO, LULC) used
903 in this study are archived on Zenodo (<https://doi.org/10.5281/zenodo.6484857>).

904

905 *Author contributions.* LCL designed and conducted the experiments, analyzed model outputs, and
906 drafted the manuscript. GB designed the study, interpreted the results, and improved the
907 manuscript. LRL contributed to the interpretation and discussion of results and improvement of
908 the manuscript.

909

910 *Acknowledgments.* This research was conducted at Pacific Northwest National Laboratory,
911 operated for the U.S. Department of Energy by Battelle Memorial Institute under contract DE-
912 AC05-76RL01830. This study is supported by the US Department of Energy (DOE) Office of
913 Science Biological and Environmental Research as part of the Regional and Global Model
914 Analysis (RGMA) program area through the collaborative, multi-program Integrated Coastal
915 Modeling (ICoM) project. This study used DOE's Biological and Environmental Research Earth
916 System Modeling program's Compy computing cluster located at Pacific Northwest National
917 Laboratory. We also want to thank the reviewers for their informative and constructive comments
918 and suggestions.

919

920 *Competing interests.* The authors declare that they have no conflict of interest.

Deleted: *Code and data availability.* The source code of ELMv1 is available from (last access: September 2020); NLDAS-2 forcing is available from <https://ldas.gsfc.nasa.gov/nldas/v2/forcing>; SOIL and TOPO related datasets are downloaded from <https://svn-ccsm-inputdata.cgd.ucar.edu/trunk/inputdata/lnd/clm2/rawdata/>; LULC related datasets are from Ke et al. (2012); ERA5-Land reanalysis is available from: <https://cds.climate.copernicus.eu/cdsapp#!/dataset/reanalysis-era5-land-monthly-means?tab=overview>.⁴

931 **Reference**

932

- 933 Avissar, R. and Pielke, R. A.: A Parameterization of Heterogeneous Land Surfaces for
934 Atmospheric Numerical Models and Its Impact on Regional Meteorology, *Mon Weather Rev*,
935 117, 2113–2136, [https://doi.org/10.1175/1520-0493\(1989\)117<2113:apohls>2.0.co;2](https://doi.org/10.1175/1520-0493(1989)117<2113:apohls>2.0.co;2), 1989.
- 936 Batjes, N. H.: Harmonized soil profile data for applications at global and continental scales:
937 updates to the WISE database, *Soil Use Manage*, 25, 124–127, [https://doi.org/10.1111/j.1475-](https://doi.org/10.1111/j.1475-2743.2009.00202.x)
938 [2743.2009.00202.x](https://doi.org/10.1111/j.1475-2743.2009.00202.x), 2009.
- 939 Bierkens, M. F. P., Bell, V. A., Burek, P., Chaney, N., Condon, L. E., David, C. H., Roo, A. de,
940 Döll, P., Drost, N., Famiglietti, J. S., Flörke, M., Gochis, D. J., Houser, P., Hut, R., Keune, J.,
941 Kollet, S., Maxwell, R. M., Reager, J. T., Samaniego, L., Sudicky, E., Sutanudjaja, E. H.,
942 Giesen, N. van de, Winsemius, H., and Wood, E. F.: Hyper-resolution global hydrological
943 modelling: what is next?, 29, 310–320, <https://doi.org/10.1002/hyp.10391>, 2014.
- 944 Bisht, G., Riley, W. J., Hammond, G. E., and Lorenzetti, D. M.: Development and evaluation of
945 a variably saturated flow model in the global E3SM Land Model (ELM) version 1.0, *Geosci*
946 *Model Dev*, 11, 4085–4102, <https://doi.org/10.5194/gmd-11-4085-2018>, 2018.
- 947 Bonan, G. B., Levis, S., Kergoat, L., and Oleson, K. W.: Landscapes as patches of plant
948 functional types: An integrating concept for climate and ecosystem models, *Global Biogeochem*
949 *Cy*, 16, 5-1-5–23, <https://doi.org/10.1029/2000gb001360>, 2002.
- 950 Caldwell, P. M., Mametjanov, A., Tang, Q., Roedel, L. P. V., Golaz, J., Lin, W., Bader, D. C.,
951 Keen, N. D., Feng, Y., Jacob, R., Maltrud, M. E., Roberts, A. F., Taylor, M. A., Veneziani, M.,
952 Wang, H., Wolfe, J. D., Balaguru, K., Cameron-Smith, P., Dong, L., Klein, S. A., Leung, L. R.,
953 Li, H., Li, Q., Liu, X., Neale, R. B., Pinheiro, M., Qian, Y., Ullrich, P. A., Xie, S., Yang, Y.,
954 Zhang, Y., Zhang, K., and Zhou, T.: The DOE E3SM Coupled Model Version 1: Description and
955 Results at High Resolution, *J Adv Model Earth Sy*, 11, 4095–4146,
956 <https://doi.org/10.1029/2019ms001870>, 2019.
- 957 Chaney, N. W., Metcalfe, P., and Wood, E. F.: HydroBlocks: a field-scale resolving land surface
958 model for application over continental extents, *Hydrol Process*, 30, 3543–3559,
959 <https://doi.org/10.1002/hyp.10891>, 2016.
- 960 Chaney, N. W., Huijgevoort, M. H. J. V., Shevliakova, E., Malyshev, S., Milly, P. C. D.,
961 Gauthier, P. P. G., and Sulman, B. N.: Harnessing big data to rethink land heterogeneity in Earth
962 system models, *Hydrol Earth Syst Sc*, 22, 3311–3330, [https://doi.org/10.5194/hess-22-3311-](https://doi.org/10.5194/hess-22-3311-2018)
963 [2018](https://doi.org/10.5194/hess-22-3311-2018), 2018.
- 964 Clark, M. P., Fan, Y., Lawrence, D. M., Adam, J. C., Bolster, D., Gochis, D. J., Hooper, R. P.,
965 Kumar, M., Leung, L. R., Mackay, D. S., Maxwell, R. M., Shen, C., Swenson, S. C., and Zeng,

- 966 X.: Improving the representation of hydrologic processes in Earth System Models, 51, 5929–
967 5956, <https://doi.org/10.1002/2015wr017096>, 2015.
- 968 Cuesta-Valero, F. J., García-García, A., Beltrami, H., González-Rouco, F., and García-
969 Bustamante, E.: WRF v.3.9 sensitivity to land surface model and horizontal resolution changes
970 over North America, *Geosci Model Dev*, <https://doi.org/10.5194/gmd-2021-243>, 2020.
- 971 Dai, H., Ye, M., Walker, A. P., and Chen, X.: A new process sensitivity index to identify
972 important system processes under process model and parametric uncertainty, *Water Resour Res*,
973 53, 3476–3490, <https://doi.org/10.1002/2016wr019715>, 2017.
- 974 Essery, R. L. H., Best, M. J., Betts, R. A., Cox, P. M., and Taylor, C. M.: Explicit Representation
975 of Subgrid Heterogeneity in a GCM Land Surface Scheme, *J Hydrometeorol*, 4, 530–543,
976 [https://doi.org/10.1175/1525-7541\(2003\)004<0530:eroshi>2.0.co;2](https://doi.org/10.1175/1525-7541(2003)004<0530:eroshi>2.0.co;2), 2003.
- 977 Fan, Y., Clark, M., Lawrence, D. M., Swenson, S., Band, L. E., Brantley, S. L., Brooks, P. D.,
978 Dietrich, W. E., Flores, A., Grant, G., Kirchner, J. W., Mackay, D. S., McDonnell, J. J., Milly, P.
979 C. D., Sullivan, P. L., Tague, C., Ajami, H., Chaney, N., Hartmann, A., Hazenberg, P.,
980 McNamara, J., Pelletier, J., Perket, J., Rouholahnejad-Freund, E., Wagener, T., Zeng, X.,
981 Beighley, E., Buzan, J., Huang, M., Livneh, B., Mohanty, B. P., Nijssen, B., Safeeq, M., Shen,
982 C., Verseveld, W., Volk, J., and Yamazaki, D.: Hillslope Hydrology in Global Change Research
983 and Earth System Modeling, *Water Resour Res*, 55, 1737–1772,
984 <https://doi.org/10.1029/2018wr023903>, 2019.
- 985 Fang, Y., Leung, L. R., Duan, Z., Wigmosta, M. S., Maxwell, R. M., Chambers, J. Q., and
986 Tomasella, J.: Influence of landscape heterogeneity on water available to tropical forests in an
987 Amazonian catchment and implications for modeling drought response, 122, 8410–8426,
988 <https://doi.org/10.1002/2017jd027066>, 2017.
- 989 Fang, Y., Leung, L. R., Wolfe, B. T., Detto, M., Knox, R. G., McDowell, N. G., Grossiord, C.,
990 Xu, C., Christoffersen, B. O., Gentine, P., Koven, C. D., and Chambers, J. Q.: Disentangling the
991 Effects of Vapor Pressure Deficit and Soil Water Availability on Canopy Conductance in a
992 Seasonal Tropical Forest During the 2015 El Niño Drought, *J Geophys Res Atmospheres*, 126,
993 <https://doi.org/10.1029/2021jd035004>, 2021.
- 994 Findell, K. L., Berg, A., Gentine, P., Krasting, J. P., Lintner, B. R., Malyshev, S., Santanello, J.
995 A., and Shevliakova, E.: The impact of anthropogenic land use and land cover change on
996 regional climate extremes, 8, 989, <https://doi.org/10.1038/s41467-017-01038-w>, 2017.
- 997 Fisher, R. A. and Koven, C. D.: Perspectives on the Future of Land Surface Models and the
998 Challenges of Representing Complex Terrestrial Systems, *J Adv Model Earth Sy*, 12,
999 <https://doi.org/10.1029/2018ms001453>, 2020.
- 1000 Garnaud, C., Bélair, S., Berg, A., and Rowlandson, T.: Hyperresolution Land Surface Modeling
1001 in the Context of SMAP Cal–Val, *J Hydrometeorol*, 17, 345–352, <https://doi.org/10.1175/jhm-d-15-0070.1>, 2016.

- 1003 Giorgi, F. and Avissar, R.: Representation of heterogeneity effects in Earth system modeling:
1004 Experience from land surface modeling, *Rev Geophys*, 35, 413–437,
1005 <https://doi.org/10.1029/97rg01754>, 1997.
- 1006 Hao, D., Bisht, G., Gu, Y., Lee, W., Liou, K.-N., and Leung, L. R.: A Parameterization of Sub-
1007 grid Topographical Effects on Solar Radiation in the E3SM Land Model (Version 1.0):
1008 Implementation and Evaluation Over the Tibetan Plateau, *Geoscientific Model Dev Discuss*,
1009 2021, 1–23, <https://doi.org/10.5194/gmd-2021-55>, 2021.
- 1010 He, S., Smirnova, T. G., and Benjamin, S. G.: Single-Column Validation of a Snow Subgrid
1011 Parameterization in the Rapid Update Cycle Land-Surface Model (RUC LSM), *Water Resour*
1012 *Res*, 57, <https://doi.org/10.1029/2021wr029955>, 2021.
- 1013 Hugelius, G., Tarnocai, C., Broll, G., Canadell, J. G., Kuhry, P., and Swanson, D. K.: The
1014 Northern Circumpolar Soil Carbon Database: spatially distributed datasets of soil coverage and
1015 soil carbon storage in the northern permafrost regions, *Earth Syst Sci Data*, 5, 3–13,
1016 <https://doi.org/10.5194/essd-5-3-2013>, 2013.
- 1017 Ji, P., Yuan, X., and Liang, X.: Do Lateral Flows Matter for the Hyperresolution Land Surface
1018 Modeling?, *J Geophys Res Atmospheres*, 122, 12,077–12,092,
1019 <https://doi.org/10.1002/2017jd027366>, 2017.
- 1020 Jr., J. A. S., Dirmeyer, P. A., Ferguson, C. R., Findell, K. L., Tawfik, A. B., Berg, A., Ek, M.,
1021 Gentine, P., Guillod, B. P., Heerwaarden, C. van, Roundy, J., and Wulfmeyer, V.: Land-
1022 Atmosphere Interactions: The LoCo Perspective, *B Am Meteorol Soc*, 99, 1253–1272,
1023 <https://doi.org/10.1175/bams-d-17-0001.1>, 2017.
- 1024 Ke, Y., Leung, L. R., Huang, M., Coleman, A. M., Li, H., and Wigmosta, M. S.: Development of
1025 high resolution land surface parameters for the Community Land Model, *Geosci Model Dev*, 5,
1026 1341–1362, <https://doi.org/10.5194/gmd-5-1341-2012>, 2012.
- 1027 Ko, A., Mascaro, G., and Vivoni, E. R.: Strategies to Improve and Evaluate Physics-Based
1028 Hyperresolution Hydrologic Simulations at Regional Basin Scales, *Water Resour Res*, 55, 1129–
1029 1152, <https://doi.org/10.1029/2018wr023521>, 2019.
- 1030 Koster, R. D., Hahmann, A. N., Ijpeelaar, R., Tyahla, L., Suarez, M. J., Dirmeyer, P. A.,
1031 Hahmann, A. N., Ijpeelaar, R., Tyahla, L., Cox, P., and Suarez, M. J.: Comparing the Degree of
1032 Land–Atmosphere Interaction in Four Atmospheric General Circulation Models, 3, 363–375,
1033 [https://doi.org/10.1175/1525-7541\(2002\)003<0363:ctdola>2.0.co;2](https://doi.org/10.1175/1525-7541(2002)003<0363:ctdola>2.0.co;2), 2002.
- 1034 Krakauer, N. Y., Li, H., and Fan, Y.: Groundwater flow across spatial scales: importance for
1035 climate modeling, *Environ Res Lett*, 9, 034003, <https://doi.org/10.1088/1748-9326/9/3/034003>,
1036 2014.
- 1037 Lawrence, D. M. and Slater, A. G.: Incorporating organic soil into a global climate model, *Clim*
1038 *Dynam*, 30, 145–160, <https://doi.org/10.1007/s00382-007-0278-1>, 2008.

- 1039 Lawrence, D. M., Fisher, R. A., Koven, C. D., Oleson, K. W., Swenson, S. C., Bonan, G.,
 1040 Collier, N., Ghimire, B., Kampenhout, L., Kennedy, D., Kluzek, E., Lawrence, P. J., Li, F., Li,
 1041 H., Lombardozzi, D., Riley, W. J., Sacks, W. J., Shi, M., Vertenstein, M., Wieder, W. R., Xu, C.,
 1042 Ali, A. A., Badger, A. M., Bisht, G., Broeke, M., Brunke, M. A., Burns, S. P., Buzan, J., Clark,
 1043 M., Craig, A., Dahlin, K., Drewniak, B., Fisher, J. B., Flanner, M., Fox, A. M., Gentine, P.,
 1044 Hoffman, F., Keppel-Aleks, G., Knox, R., Kumar, S., Lenaerts, J., Leung, L. R., Lipscomb, W.
 1045 H., Lu, Y., Pandey, A., Pelletier, J. D., Perket, J., Randerson, J. T., Ricciuto, D. M., Sanderson,
 1046 B. M., Slater, A., Subin, Z. M., Tang, J., Thomas, R. Q., Martin, M. V., and Zeng, X.: The
 1047 Community Land Model Version 5: Description of New Features, Benchmarking, and Impact of
 1048 Forcing Uncertainty, *J Adv Model Earth Sy*, 11, 4245–4287,
 1049 <https://doi.org/10.1029/2018ms001583>, 2019.
- 1050 Lawrence, P. J. and Chase, T. N.: Representing a new MODIS consistent land surface in the
 1051 Community Land Model (CLM 3.0), *J Geophys Res Biogeosciences* 2005 2012, 112,
 1052 <https://doi.org/10.1029/2006jg000168>, 2007.
- 1053 Leung, L. R., Bader, D. C., Taylor, M. A., and McCoy, R. B.: An Introduction to the E3SM
 1054 Special Collection: Goals, Science Drivers, Development, and Analysis, *J Adv Model Earth Sy*,
 1055 12, <https://doi.org/10.1029/2019ms001821>, 2020.
- 1056 Li, H., Wigmosta, M. S., Wu, H., Huang, M., Ke, Y., Coleman, A. M., and Leung, L. R.: A
 1057 Physically Based Runoff Routing Model for Land Surface and Earth System Models, *J*
 1058 *Hydrometeorol*, 14, 808–828, <https://doi.org/10.1175/jhm-d-12-015.1>, 2013a.
- 1059 Li, J., Duan, Q. Y., Gong, W., Ye, A., Dai, Y., Miao, C., Di, Z., Tong, C., and Sun, Y.:
 1060 Assessing parameter importance of the Common Land Model based on qualitative and
 1061 quantitative sensitivity analysis, *Hydrol Earth Syst Sc*, 17, 3279–3293,
 1062 <https://doi.org/10.5194/hess-17-3279-2013>, 2013b.
- 1063 Li, L., Zhang, L., Xia, J., Gippel, C. J., Wang, R., and Zeng, S.: Implications of Modelled
 1064 Climate and Land Cover Changes on Runoff in the Middle Route of the South to North Water
 1065 Transfer Project in China, 29, 2563–2579, <https://doi.org/10.1007/s11269-015-0957-3>, 2015.
- 1066 Li, L., She, D., Zheng, H., Lin, P., and Yang, Z. L.: Elucidating Diverse Drought Characteristics
 1067 from Two Meteorological Drought Indices (SPI and SPEI) in China, 21, 1513–1530,
 1068 <https://doi.org/10.1175/jhm-d-19-0290.1>, 2020.
- 1069 Li, L., Yang, Z., Matheny, A. M., Zheng, H., Swenson, S. C., Lawrence, D. M., Barlage, M.,
 1070 Yan, B., McDowell, N. G., and Leung, L. R.: Representation of Plant Hydraulics in the Noah-
 1071 MP Land Surface Model: Model Development and Multiscale Evaluation, *J Adv Model Earth*
 1072 *Sy*, 13, <https://doi.org/10.1029/2020ms002214>, 2021.
- 1073 Li, Y., Piao, S., Li, L. Z. X., Chen, A., and Zhou, L.: Divergent hydrological response to large-
 1074 scale afforestation and vegetation greening in China, 4, eaar4182,
 1075 <https://doi.org/10.1126/sciadv.aar4182>, 2018.

- 1076 Lindstedt, D., Lind, P., Kjellström, E., and Jones, C.: A new regional climate model operating at
 1077 the meso-gamma scale: performance over Europe, *Tellus*, 67, 24138,
 1078 <https://doi.org/10.3402/tellusa.v67.24138>, 2015.
- 1079 Liu, S., Shao, Y., Kunoth, A., and Simmer, C.: Impact of surface-heterogeneity on atmosphere
 1080 and land-surface interactions, *Environ Modell Softw*, 88, 35–47,
 1081 <https://doi.org/10.1016/j.envsoft.2016.11.006>, 2017.
- 1082 Maxwell, R. M., Condon, L. E., and Kollet, S. J.: A high-resolution simulation of groundwater
 1083 and surface water over most of the continental US with the integrated hydrologic model ParFlow
 1084 v3, *Geosci Model Dev*, 8, 923–937, <https://doi.org/10.5194/gmd-8-923-2015>, 2015.
- 1085 Muñoz-Sabater, J., Dutra, E., Agustí-Panareda, A., Albergel, C., Arduini, G., Balsamo, G.,
 1086 Boussetta, S., Choulga, M., Harrigan, S., Hersbach, H., Martens, B., Miralles, D. G., Piles, M.,
 1087 Rodríguez-Fernández, N. J., Zsoter, E., Buontempo, C., and Thépaut, J.-N.: ERA5-Land: a state-
 1088 of-the-art global reanalysis dataset for land applications, *Earth Syst Sci Data*, 13, 4349–4383,
 1089 <https://doi.org/10.5194/essd-13-4349-2021>, 2021.
- 1090 Naz, B. S., Kurtz, W., Montzka, C., Sharples, W., Goergen, K., Keune, J., Gao, H., Springer, A.,
 1091 Franssen, H.-J. H., and Kollet, S.: Improving soil moisture and runoff simulations at 3 km over
 1092 Europe using land surface data assimilation, *Hydrol Earth Syst Sc*, 23, 277–301,
 1093 <https://doi.org/10.5194/hess-23-277-2019>, 2018.
- 1094 Nossent, J., Elsen, P., and Bauwens, W.: **Sobol'** sensitivity analysis of a complex environmental
 1095 model, *Environ Modell Softw*, 26, 1515–1525, <https://doi.org/10.1016/j.envsoft.2011.08.010>,
 1096 2011.
- 1097 PIELKE, R. A., ADEGOKE, J., BELTRÁN-PRZEKURAT, A., HIEMSTRA, C. A., LIN, J.,
 1098 NAIR, U. S., NIYOGLI, D., and NOBIS, T. E.: An overview of regional land-use and land-cover
 1099 impacts on rainfall, *Tellus B*, 59, 587–601, <https://doi.org/10.1111/j.1600-0889.2007.00251.x>,
 1100 2007.
- 1101 Rosolem, R., Gupta, H. V., Shuttleworth, W. J., Zeng, X., and Gonçalves, L. G. G.: A fully
 1102 multiple-criteria implementation of the Sobol' method for parameter sensitivity analysis, *J*
 1103 *Geophys Res Atmospheres* 117, n/a-n/a, <https://doi.org/10.1029/2011jd016355>,
 1104 2012.
- 1105 Rouf, T., Maggioni, V., Mei, Y., and Houser, P.: Towards hyper-resolution land-surface
 1106 modeling of surface and root zone soil moisture, *J Hydrol*, 594, 125945,
 1107 <https://doi.org/10.1016/j.jhydrol.2020.125945>, 2021.
- 1108 Rummukainen, M.: Added value in regional climate modeling, *Wiley Interdiscip Rev Clim*
 1109 *Change*, 7, 145–159, <https://doi.org/10.1002/wcc.378>, 2016.
- 1110 Saltelli, A.: Sensitivity Analysis for Importance Assessment, *Risk Anal*, 22, 579–590,
 1111 <https://doi.org/10.1111/0272-4332.00040>, 2002.

Deleted: Sobol'

- 1113 Saltelli, A., Annoni, P., Azzini, I., Campolongo, F., Ratto, M., and Tarantola, S.: Variance based
 1114 sensitivity analysis of model output. Design and estimator for the total sensitivity index, *Comput*
 1115 *Phys Commun*, 181, 259–270, <https://doi.org/10.1016/j.cpc.2009.09.018>, 2010.
- 1116 Saltelli, A., Aleksankina, K., Becker, W., Fennell, P., Ferretti, F., Holst, N., Li, S., and Wu, Q.:
 1117 Why so many published sensitivity analyses are false: A systematic review of sensitivity analysis
 1118 practices, *Environ Modell Softw*, 114, 29–39, <https://doi.org/10.1016/j.envsoft.2019.01.012>,
 1119 2019.
- 1120 Scheidegger, J. M., Jackson, C. R., Muddu, S., Tomer, S. K., and Filgueira, R.: Integration of 2D
 1121 Lateral Groundwater Flow into the Variable Infiltration Capacity (VIC) Model and Effects on
 1122 Simulated Fluxes for Different Grid Resolutions and Aquifer Diffusivities, *Water-sui*, 13, 663,
 1123 <https://doi.org/10.3390/w13050663>, 2021.
- 1124 Simon, J. S., Bragg, A. D., Dirmeyer, P. A., and Chaney, N. W.: Semi-coupling of a Field-scale
 1125 Resolving Land-surface Model and WRF-LES to Investigate the Influence of Land-surface
 1126 Heterogeneity on Cloud Development, <https://doi.org/10.1002/essoar.10507168.1>, 2020.
- 1127 Singh, R. S., Reager, J. T., Miller, N. L., and Famiglietti, J. S.: Toward hyper-resolution land-
 1128 surface modeling: The effects of fine-scale topography and soil texture on CLM4.0 simulations
 1129 over the Southwestern U.S., *Water Resour Res*, 51, 2648–2667,
 1130 <https://doi.org/10.1002/2014wr015686>, 2015.
- 1131 Swann, A. L., Fung, I. Y., Levis, S., Bonan, G. B., and Doney, S. C.: Changes in Arctic
 1132 vegetation amplify high-latitude warming through the greenhouse effect., 107, 1295–1300,
 1133 <https://doi.org/10.1073/pnas.0913846107>, 2010.
- 1134 Swenson, S. C., Clark, M., Fan, Y., Lawrence, D. M., and Perket, J.: Representing Intrahillslope
 1135 Lateral Subsurface Flow in the Community Land Model, *J Adv Model Earth Sy*, 11, 4044–4065,
 1136 <https://doi.org/10.1029/2019ms001833>, 2019.
- 1137 Taylor, R. G., Scanlon, B., Döll, P., Rodell, M., Beek, R. van, Wada, Y., Longuevergne, L.,
 1138 Leblanc, M., Famiglietti, J. S., Edmunds, M., Konikow, L., Green, T. R., Chen, J., Taniguchi,
 1139 M., Bierkens, M. F., MacDonald, A., Fan, Y., Maxwell, R. M., Yecheili, Y., Gurdak, J. J., Allen,
 1140 D. M., Shamsudduha, M., Hiscock, K., Yeh, P., Holman, I., and Treidel, H.: Ground water and
 1141 climate change, 3, 322–329, <https://doi.org/10.1038/nclimate1744>, 2012.
- 1142 Tesfa, T. K. and Leung, L.-Y. R.: Exploring new topography-based subgrid spatial structures for
 1143 improving land surface modeling, *Geosci Model Dev*, 10, 873–888, <https://doi.org/10.5194/gmd-10-873-2017>, 2017.
- 1145 Tesfa, T. K., Leung, L. R., Huang, M., Li, H., Voisin, N., and Wigmosta, M. S.: Scalability of
 1146 grid- and subbasin-based land surface modeling approaches for hydrologic simulations, *J*
 1147 *Geophys Res Atmospheres*, 119, 3166–3184, <https://doi.org/10.1002/2013jd020493>, 2014.

1148 Tesfá, T. K., Leung, L. R., and Ghan, S. J.: Exploring Topography-Based Methods for
1149 Downscaling Subgrid Precipitation for Use in Earth System Models, *J Geophys Res*
1150 *Atmospheres*, 125, <https://doi.org/10.1029/2019jd031456>, 2020.

1151 Torma, C., Giorgi, F., and Coppola, E.: Added value of regional climate modeling over areas
1152 characterized by complex terrain—Precipitation over the Alps, *J Geophys Res Atmospheres*,
1153 120, 3957–3972, <https://doi.org/10.1002/2014jd022781>, 2015.

1154 Vegas-Cañas, C., González-Rouco, J. F., Navarro-Montesinos, J., García-Bustamante, E., Lucio-
1155 Eceiza, E. E., García-Pereira, F., Rodríguez-Camino, E., Chazarra-Bernabé, A., and Álvarez-
1156 Arévalo, I.: An Assessment of Observed and Simulated Temperature Variability in Sierra de
1157 Guadarrama, *Atmosphere-basel*, 11, 985, <https://doi.org/10.3390/atmos11090985>, 2020.

1158 Vergopolan, N., Chaney, N. W., Beck, H. E., Pan, M., Sheffield, J., Chan, S., and Wood, E. F.:
1159 Combining hyper-resolution land surface modeling with SMAP brightness temperatures to
1160 obtain 30-m soil moisture estimates, *Remote Sens Environ*, 242, 111740,
1161 <https://doi.org/10.1016/j.rse.2020.111740>, 2020.

1162 Xia, Y., Mitchell, K., Ek, M., Cosgrove, B., Sheffield, J., Luo, L., Alonge, C., Wei, H., Meng, J.,
1163 Livneh, B., Duan, Q., and Lohmann, D.: Continental-scale water and energy flux analysis and
1164 validation for North American Land Data Assimilation System project phase 2 (NLDAS-2): 2.
1165 Validation of model-simulated streamflow, *J Geophys Res Atmospheres* 117, 117,
1166 <https://doi.org/10.1029/2011jd016051>, 2012a.

1167 Xia, Y., Mitchell, K., Ek, M., Sheffield, J., Cosgrove, B., Wood, E., Luo, L., Alonge, C., Wei,
1168 H., Meng, J., Livneh, B., Lettenmaier, D., Koren, V., Duan, Q., Mo, K., Fan, Y., and Mocko, D.:
1169 Continental-scale water and energy flux analysis and validation for the North American Land
1170 Data Assimilation System project phase 2 (NLDAS-2): 1. Intercomparison and application of
1171 model products: WATER AND ENERGY FLUX ANALYSIS, *J Geophys Res Atmospheres*,
1172 117, n/a-n/a, <https://doi.org/10.1029/2011jd016048>, 2012b.

1173 Xie, Z., Wang, L., Wang, Y., Liu, B., Li, R., Xie, J., Zeng, Y., Liu, S., Gao, J., Chen, S., Jia, B.,
1174 and Qin, P.: Land Surface Model CAS-LSM: Model Description and Evaluation, *J Adv Model*
1175 *Earth Sy*, 12, <https://doi.org/10.1029/2020ms002339>, 2020.

1176 Xu, C., McDowell, N. G., Fisher, R. A., Wei, L., Sevanto, S., Christoffersen, B. O., Weng, E.,
1177 and Middleton, R. S.: Increasing impacts of extreme droughts on vegetation productivity under
1178 climate change, *Nat Clim Change*, 9, 948–953, <https://doi.org/10.1038/s41558-019-0630-6>,
1179 2019.

1180 Xue, Y., Houser, P. R., Maggioni, V., Mei, Y., Kumar, S. V., and Yoon, Y.: Evaluation of High
1181 Mountain Asia-Land Data Assimilation System (Version 1) From 2003 to 2016, Part I: A Hyper-
1182 Resolution Terrestrial Modeling System, *J Geophys Res Atmospheres*, 126,
1183 <https://doi.org/10.1029/2020jd034131>, 2021.

- 1184 Yang, X., Ricciuto, D. M., Thornton, P. E., Shi, X., Xu, M., Hoffman, F., and Norby, R. J.: The
1185 Effects of Phosphorus Cycle Dynamics on Carbon Sources and Sinks in the Amazon Region: A
1186 Modeling Study Using ELM v1, *J Geophys Res Biogeosciences*, 124, 3686–3698,
1187 <https://doi.org/10.1029/2019jg005082>, 2019.
- 1188 Yuan, K., Zhu, Q., Zheng, S., Zhao, L., Chen, M., Riley, W. J., Cai, X., Ma, H., Li, F., Wu, H.,
1189 and Chen, L.: Deforestation reshapes land-surface energy-flux partitioning, *Environ Res Lett*, 16,
1190 024014, <https://doi.org/10.1088/1748-9326/abd8f9>, 2021.
- 1191 Yuan, W., Zheng, Y., Piao, S., Ciais, P., Lombardozzi, D., Wang, Y., Ryu, Y., Chen, G., Dong,
1192 W., Hu, Z., Jain, A. K., Jiang, C., Kato, E., Li, S., Lienert, S., Liu, S., Nabel, J. E. M. S., Qin, Z.,
1193 Quine, T., Sitch, S., Smith, W. K., Wang, F., Wu, C., Xiao, Z., and Yang, S.: Increased
1194 atmospheric vapor pressure deficit reduces global vegetation growth, 5, *eaax1396*,
1195 <https://doi.org/10.1126/sciadv.aax1396>, 2019.
- 1196 Yuan, X., Ji, P., Wang, L., Liang, X., Yang, K., Ye, A., Su, Z., and Wen, J.: High-Resolution
1197 Land Surface Modeling of Hydrological Changes Over the Sanjiangyuan Region in the Eastern
1198 Tibetan Plateau: 1. Model Development and Evaluation, *J Adv Model Earth Sy*, 10, 2806–2828,
1199 <https://doi.org/10.1029/2018ms001412>, 2018.
- 1200 Zeng, Z., Piao, S., Li, L., Zhou, L., CIAIS, P., and Wang, T.: Climate mitigation from vegetation
1201 biophysical feedbacks during the past three decades, 2017.
- 1202 Zhang, X., Trame, M., Lesko, L., and Schmidt, S.: Sobol Sensitivity Analysis: A Tool to Guide
1203 the Development and Evaluation of Systems Pharmacology Models, *Cpt Pharmacometrics Syst*
1204 *Pharmacol*, 4, 69–79, <https://doi.org/10.1002/psp4.6>, 2015.
- 1205 Zheng, H., Yang, Z., Lin, P., Wei, J., Wu, W., Li, L., Zhao, L., and Wang, S.: On the Sensitivity
1206 of the Precipitation Partitioning Into Evapotranspiration and Runoff in Land Surface
1207 Parameterizations, *Water Resour Res*, 55, 95–111, <https://doi.org/10.1029/2017wr022236>, 2019.
- 1208 Zhou, T., Leung, L. R., Leng, G., Voisin, N., Li, H., Craig, A. P., Tesfa, T., and Mao, Y.: Global
1209 Irrigation Characteristics and Effects Simulated by Fully Coupled Land Surface, River, and
1210 Water Management Models in E3SM, *J Adv Model Earth Sy*, 12,
1211 <https://doi.org/10.1029/2020ms002069>, 2020.
- 1212 Zhou, Y., Li, D., and Li, X.: The Effects of Surface Heterogeneity Scale on the Flux Imbalance
1213 under Free Convection, *J Geophys Res Atmospheres*, 124, 8424–8448,
1214 <https://doi.org/10.1029/2018jd029550>, 2019.
- 1215